



21 **Abstract**

22 Ocean alkalinity enhancement (OAE) is a strategy for marine carbon dioxide removal that aims to increase the  
23 total alkalinity (TA) of seawater to sequester atmospheric CO<sub>2</sub> in the form of dissolved inorganic carbon (DIC). An  
24 intense alkalization of seawater resulting from OAE treatment could trigger a significant runaway carbonate  
25 precipitation process, which may lead to a loss of initially added TA, thereby limiting its efficiency. Even under  
26 natural background aragonite saturation states, a continuous yet barely detectable loss of TA is theoretically  
27 expected to occur in seawater. With the additional increase through OAE, time ranges to initiate an appreciable  
28 TA-loss process could be reduced significantly. Therefore, predicting the TA stability ranges might be a necessity  
29 for application scenarios. The main drivers of the precipitation process are i) the aragonite saturation state of  
30 seawater and ii) the available surface area for heterogeneous precipitation.

31 In this study, we refined the use of logistic functions to describe the temporal evolution of both drivers, with  
32 experimental datasets using natural seawater from the Raunefjorden (Bergen, Norway; Temp.: ~11°C, Sal.:  
33 ~32.6). The observed patterns were then used to derive a process-based model for calculating TA-loss rates,  
34 focusing on the accelerated precipitation phase of the runaway process while considering saturation levels and  
35 available particle surface area. The formation of carbonate phases reduces seawater TA concentrations, inducing  
36 a delay or ~~stopping-halting~~ the TA-loss process. In addition, the sinking of precipitated particles decreases the  
37 potential for further precipitation by reducing the available surface area in the system. To assess the impact of  
38 particle sinking on TA-loss, their shape and size distribution were determined. Under the environmental  
39 conditions presented here, TA-loss rates could be reduced by up to 30-40% due to the sinking of particles, after  
40 just one day.

41 Integrating the proposed concepts into ocean models could enhance the accuracy of predictions regarding the  
42 fate of added TA. Gaining insights into the evolution of the identified, seemingly stable TA levels can help prevent  
43 accelerated precipitation phases. Additionally, an understanding of particle sinking or dilution processes,  
44 reducing the available reactive particle surface area, is relevant to assess the efficacy and durability of OAE.

45

## 46 1 Introduction

47 To mitigate climate change and reach net-zero greenhouse gas emissions by the end of the century, negative  
48 emission technologies (NETs) are necessary besides greenhouse gas emission reduction (UNFCCC, 2015)  
49 considering the slow change in the development of the energy infrastructure, lifestyle of humanity, and national  
50 goals for economic growth (Fuss et al., 2018; Iyer et al., 2015; Sers & Victor, 2018). Various carbon dioxide  
51 removal (CDR) technologies have been proposed to help achieve the necessary negative emission trajectories  
52 (Hartmann et al., 2013; IPCC, 2023; Minx et al., 2018; Rogelj et al., 2018). Among these, ocean alkalinity  
53 enhancement (OAE) is a promising CDR method (Harvey, 2008; Ilyina et al., 2013; Kheshti, 1995; Rau & Caldeira,  
54 1999), with the potential to geochemically sequester 3-30 Gt CO<sub>2</sub> yr<sup>-1</sup> (Oschlies et al., 2023; Renforth &  
55 Henderson, 2017).

56 Enhancing total alkalinity (TA) could be achieved by two ~~addition~~ approaches: **1.** a non-CO<sub>2</sub>-equilibrated (neq) or  
57 **2.** a CO<sub>2</sub>-equilibrated (eq) (Schulz et al., 2023). Through the neq approach, alkaline materials, such as silicate or  
58 hydroxide-based mineral phases, could be introduced to seawater in the form of solids or solutions, allowing  
59 longer-term CO<sub>2</sub> equilibration with the atmosphere through ingassing of atmospheric CO<sub>2</sub>. In the eq approach,  
60 already partially pre-CO<sub>2</sub>-equilibrated solutions or carbonate-based substances could be released into seawater.  
61 Neq TA addition strategies induce greater variations in the affected carbonate system, resulting in drastically  
62 reduced *p*CO<sub>2</sub> and a rapid increase in pH values. While an eq TA addition results in less severe changes in ocean  
63 chemistry, it is less efficient in generating carbon sequestration potential (Schulz et al., 2023; Suitner et al., 2024).  
64 Depending on the introduced alkalization method (see Eisaman et al., 2023) and the magnitude of treatment,  
65 induced changes in the carbonate system could lead to adverse effects on biota (e.g. Faucher et al., 20254;  
66 Ferderer et al., 2022; Gately et al., 2023; Goldenberg et al., 2024; Marín-Samper et al., 2024; Sánchez et al., 2024;  
67 Xin et al., 2024) or in case of persistent oversaturation, result in the precipitation of secondary mineral phases  
68 and therefore a loss of the introduced TA (Ilyina et al., 2013; Schulz et al., 2023). The process of TA leakage as a  
69 consequence of OAE was recently described by several studies (see Fuhr et al., 2022; Hartmann et al., 2023;  
70 Moras et al., 2022; Pan et al., 2021; Ringham et al., 2024; Suitner et al., 2024; Varliero et al., 2024). Within these  
71 laboratory-based studies, self-sustaining runaway carbonate precipitation processes led to a significant decrease  
72 in the added TA, which could even result in a net-loss of TA. TA stability ranges, and the evolution of the  
73 precipitation process depend on the specific local environmental conditions such as temperature, salinity,  
74 aragonite saturation state ( $\Omega_{ar}$ ), or suspended particle load of the treated water mass (Moras et al., 2024).

75 ~~The objective of this study is to demonstrate the a general capability to predict and parametrize the temporal~~  
76 ~~evolution of a triggered runaway carbonate precipitation process during OAE approaches, based using on~~  
77 ~~quantifiable and measurable parameters. Stability ranges for the permanence of introduced TA additions were~~  
78 ~~derived from these parametrizations, enabling the prevention of secondary mineral formation and the~~  
79 ~~optimization of future OAE application scenarios. Estimations of stability ranges for the permanence of~~  
80 ~~introduced TA additions were derived from these parametrizations. The ability to predict TA stability ranges can~~  
81 ~~help prevent secondary mineral formation and optimize assessments for future OAE application scenarios.~~

82 ~~Suitner et al. (2024) demonstrated the potential of utilizing inverse logistic functions to depict the temporal~~  
83 ~~evolution of the TA-loss process during the runaway carbonate formation phase (see Fig. 1). Suitner et al. (2024)~~  
84 ~~demonstrated the potential of inverse logistic functions to describe the temporal evolution of TA loss during the~~  
85 ~~runaway carbonate formation phase (see Fig. 1). Building on this concept, this study presents a proof-of-concept~~  
86 ~~mechanistic kinetic framework that combines empirically derived rate equations with measurable parameters~~  
87 ~~(such as carbonate saturation state and particle surface area) to reconstruct the temporal evolution of the TA~~  
88 ~~loss and identify the main drivers of the process. The resulting parameterization is currently only calibrated to~~  
89 ~~the experimental dataset and does not yet include additional environmental controls such as temperature,~~  
90 ~~salinity, or suspended particles, but it provides a transferable calculation scheme that could later be~~  
91 ~~implemented in predictive ocean models simulating OAE addition scenarios, as discussed by He & Tyka (2023),~~  
92 ~~Ou et al. (2025), Schwinger et al. (2024), and Zhou et al. (2024).~~

93 ~~In this study, principal descriptive parameters such as TA addition and stability ranges to trigger the runaway~~  
94 ~~process or the timespan of the precipitation phase could be formalized based on their experimental dataset. This~~  
95 ~~approach also offers the possibility of a straightforward integration of time-dependent loss terms into predictive~~  
96 ~~computational models simulating OAE addition scenarios, as presented by He & Tyka (2023), Ou et al. (2025),~~  
97 ~~Schwinger et al. (2024) or Zhou et al. (2024).~~

98 The application of OAE may exceed critical levels for carbonate precipitation. For open ocean scenarios the rapid  
99 initiation of mixing processes would efficiently reduce the potential for secondary carbonate formation.  
100 Nevertheless, runaway carbonate formation may occur within enclosed geographic locations with physical  
101 features such as bays, estuaries, or lagoons. In addition, thermohaline layering (Bialik et al., 2022) or high  
102 sediment load (Wurgaft et al., 2016, 2021) might create conditions that lead to TA-loss processes.

103 To sustain a triggered runaway carbonate formation (Fig. 1), it is necessary to retain the precipitates in the  
104 system. Removal of these particles reduces the potential for continuous heterogeneous precipitation, thereby  
105 slowing down or halting the process. In this study, the empirically determined TA-loss rates were used to derive  
106 the quantity of precipitated particles. By identifying the particle sizes, shapes, densities, and sinking velocities,  
107 their potential residence times in the water column were estimated. Furthermore, we evaluated whether the  
108 formation of secondary minerals can supply sufficient surface area for a continuous detectable heterogeneous  
109 runaway process in an open-water body and whether the process would be interrupted or attenuated by  
110 removing particles due to their descent into deeper layers.

111

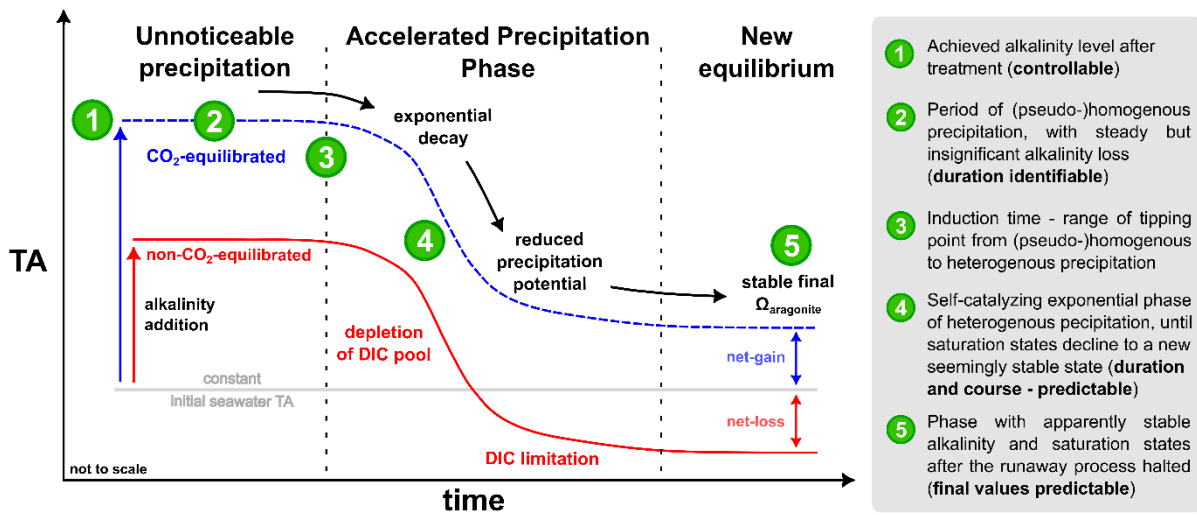


Figure 1: Modified conceptual scheme of a runaway carbonate precipitation process following liquid TA addition after Fig. 9 in Suitner et al., 2024 (not to scale).

## 113 2 Material and methods

### 114 2.1 Overview of experimental setups

115 All data analyzed in the present study derive from TA-gradient experiments described in Suitner et al. (2024).  
116 During a field study from May to July 2022-, natural seawater was collected at the Espeland marine station  
117 (Raunefjorden, Bergen, Norway; 60.27° N, 5.20° E). Within 20-25 days lasting TA-gradient approaches, 250 ml  
118 polystyrene cell culture bottles were filled with “filtered” (mesh size 0.2 μm) or “unfiltered” (mesh size 50 μm)  
119 natural seawater ( $TA_{initial} \sim 2190 \pm 10 \mu\text{mol kg}^{-1}$ ,  $DIC \sim 1890 \pm 20 \mu\text{mol kg}^{-1}$ ,  $pH \sim 8.25 \pm 0.05$ ,  $\Omega_{ar} 2.8 \pm 0.4$  and  $Sal.$   
120  $\sim 32.6 \pm 0.1$ ) and incubated in a PMMA flow-through incubation box, mimicking the natural light and temperature  
121 conditions (10-16°C). Each TA level was distributed among 3-4 bottles to allow sequential sampling while  
122 minimizing head-space. TA was either increased with a 0.5 M NaOH (neq) or with a mix of 0.4 M  
123 NaHCO<sub>3</sub> and 0.2 M Na<sub>2</sub>CO<sub>3</sub> (eq) stock solutions to maintain ambient pCO<sub>2</sub> levels ( $\sim 420 \mu\text{atm}$ ). TA, pH, salinity,  
124 conductivity and temperature were measured using a Metrohm 888 Titrando (0.02 M HCl titration) and a WTW  
125 MultiLine® multimeter. An overview of the experimental setup is given in Tab. 1; full methodological details are  
126 provided in the supplementary information (SI).

127 The precipitated particles of three selected filters (0.2 μm PC), collected during incubation experiments within  
128 previous campaigns published in Suitner et al. (2024) (neq  $\Delta TA_{2600}$  and  $\Delta TA_{2800}$ , Raunefjorden) and Hartmann et  
129 al. (2023) (neq  $\Delta TA_{2400}$ , Gran Canaria) were used to analyze particle sizes, morphology and their sinking velocities.  
130 Similar to the Raunefjorden, the filters from the Gran Canaria experiment were obtained from a TA-gradient  
131 experiment, conducted in local oligotrophic seawater ( $TA_{initial} \sim 2411 \pm 5 \mu\text{mol kg}^{-1}$ ,  $DIC \sim 2006 \pm 16 \mu\text{mol kg}^{-1}$ ,  $pH$   
132  $\sim 8.15 \pm 0.02$ ,  $\Omega_{ar} 4.4 \pm 0.3$ ,  $Sal. \sim 36.6$  Temp.  $\sim 23$  °C), designed to assess the stability of alkalization approaches  
133 (see SI for further details). Incubations during the Gran Canarian campaign ran for 4 days and followed the same  
134 analytical protocol as the Norwegian series introduced above. A detailed description of the Gran Canaria setup  
135 is provided in the SI. Three incubation experiments were conducted to examine the stability of TA of the local  
136 “filtered” (mesh size 0.2 μm) and “unfiltered” (mesh size 50 μm) seawater of the Raunefjorden, Norway (60.27°  
137 N, 5.20° E). Within TA-gradient approaches, 250 ml polystyrene cell culture bottles were filled with natural  
138 seawater and incubated in a flow through incubation box, following the natural light and temperature  
139 conditions. Runaway precipitation was observed in eq and neq treatments, after surpassing specific time and TA  
140 addition ranges, allowing the description of patterns during the precipitation process. A detailed description of  
141 the experimental results, design and methods is given in Suitner et al. (2024), a brief overview is also provided in  
142 Tab. 1 (also see SI for further details).

143  
144

Table 1: Overview of the experimental design of Raunefjorden precipitation experiments.

#	filter mesh size	CO <sub>2</sub> state to atmosphere	Alkaline material	Runtime [days]	Range TA <sub>added</sub> [μmol kg <sup>-1</sup> ]	TA <sub>added</sub> gradient steps [μmol kg <sup>-1</sup> ]	Temperature [°C]
---	------------------	-------------------------------------	-------------------	----------------	--	---	------------------

I	50 $\mu\text{m}$	non-equilibrated	NaOH	25	0-2800	200	10-11
II	0.2 $\mu\text{m}$	(neq)			0-3400		11-13
III	0.2 $\mu\text{m}$	air-equilibrated (eq)	Na <sub>2</sub> CO <sub>3</sub> / NaHCO <sub>3</sub>	20	0-9200	800	12-16

145

146 **2.2 Curve fitting of the TA and  $\Omega_{ar}$  evolution**

147 Building on [Suitner et al. \(2024\)](#), the numerical curve fit model used to describe the temporal development of  
 148 TA and  $\Omega_{ar}$ , as presented in [Suitner et al. \(2024\)](#), was refined by through the additionally including incorporation  
 149 of the observed TA-loss rates as an ~~second~~ input factor, to provide continuous functions as a basis for further  
 150 model calculations. The curve fit model utilized the consistent tendency of all observed runaway precipitation  
 151 processes to follow inverse logistic trends in form of:

$$f(t) = a e^{-b e^{-ct}} + d \quad (1)$$

152 for the temporal evolution of TA and  $\Omega_{ar}$ . The coefficients **(d)** and **(a)** are defined by the achieved level of TA/ $\Omega_{ar}$   
 153 after the addition **(d)** and the final reached value after the runaway process halted **(a)**. Since these factors are  
 154 predefined by the experimental setup, the curve fit model only numerically parameterizes the two coefficients  
 155 **(b)** and **(c)**. Coefficient **(b)** represents the “induction time”, or the time required for CaCO<sub>3</sub> precipitation to  
 156 become detectable in the TA measurements, depicted by the horizontal translation along the x-axis, while **(c)**  
 157 denotes the timespan between start and end of an accelerated precipitation phase (APP). See Fig. 2 for a visual  
 158 impression of the influence of iterations of each coefficient.  
 159

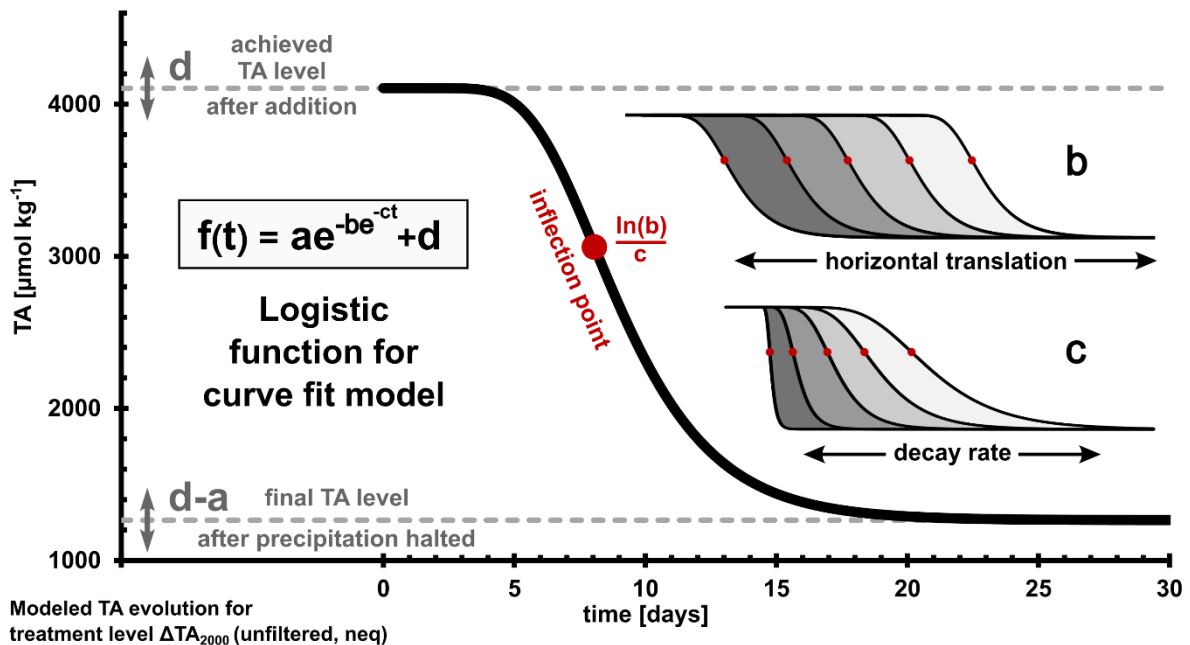


Figure 2: Overview and iterations of each coefficient **(a)-(d)** of the applied inverse logistic function for the numerical curve fitting; the inflection point is defined by  $\ln(b)/c$ ; for further characteristics see [Tjørve & Tjørve \(2017\)](#).

160

### 161 2.3 Empirical rate law and determination of loss rates

162 A simple empirical rate law was used to evaluate the precipitation rates  $R$  [ $\mu\text{mol m}^{-2} \text{h}^{-1}$ ] (see e.g. Inskeep &  
163 Bloom, 1985; Morse et al., 2007; Zhong & Mucci, 1989):

$$164 R = k(\Omega_{ar} - 1)^n \quad (2)$$

165 The experimental ~~TA-loss~~precipitation rates were then fitted to the logarithmic form of Eq. (2) to determine the  
166 coefficients  $k$  (rate constant) and  $n$  (empirical reaction order):

$$167 \log(R) = n(\Omega_{ar} - 1) + \log(k) \quad (3)$$

168 To correct for the variable surface area,  $r$  [ $\mu\text{mol h}^{-1}$ ] was normalized for the assumed available active mineral  
169 surface area ( $A$  in [ $\text{m}^2$ ]) (adapted from Sjöberg, 1976).

$$170 r = k A (\Omega_{ar} - 1)^n \quad (4)$$

171 As the gradient approaches could not provide a sufficient amount of precipitates to determine their surface area,  
172 a one-week side experiment was conducted to estimate the mineral surface area generated during the runaway  
173 precipitation process. By adding 3.8 mmol NaOH and 7.0 mmol  $\text{NaHCO}_3$  to 40 L of 0.2  $\mu\text{m}$  filtered natural  
174 seawater (salinity 33) at 23°C, around 5 g of aragonite precipitates were generated to provide material for a BET  
175 surface area measurement. Using  $\text{N}_2$  adsorption (Brunauer et al., 1938), with a Quantachrome autosorb iQ at the  
176 University of Hamburg, a surface area of  $2.283 \pm 0.018 \text{ m}^2 \text{ g}^{-1}$  was determined. By the assumption that the surface  
177 area is constant for all precipitates and that the entire lost TA is transformed into aragonite particles, the  
178 experimentally determined TA-loss was used to calculate the surface area after each timestep, therefore allowing  
179 to correct the precipitation rates.

180

### 181 2.4 Particle analysis

182 ~~Three samples of precipitates, filtered through a 0.2  $\mu\text{m}$  (PC) filter from the incubation experiments conducted~~  
183 ~~on Gran Canaria and in the Raunefjorden (see Section 2.1), were analyzed using a scanning electron microscope~~  
184 ~~(SEM; Hitachi TM4000 Plus Tabletop Microscope, University of Hamburg) to determine the morphology, size,~~  
185 ~~and relative abundance of the precipitated material. The filtered precipitates were analyzed by scanning electron~~  
186 ~~microscopy (SEM; Tabletop Microscope Hitachi TM4000plus—University of Hamburg) to determine shape, size~~  
187 ~~and quantity of the precipitated material. Length, width and shape of each particle were specified by manual~~  
188 ~~examination.~~

189 ~~When sufficient precipitated material remained following SEM analysis, the remaining SEM filter material was~~  
190 ~~used to determine their sinking velocities. were determined from the residual filter material, utilizing a~~  
191 ~~FlowCam (Fluid Imaging Technologies Inc., Scarborough, United States). A detailed description of the setup is~~  
192 ~~provided in Suessle et al. (2023) and references therein.~~

193 ~~The precipitated particles of three filters (0.2  $\mu\text{m}$  PC), collected during incubation experiments within previous~~  
194 ~~campaigns published in Hartmann et al. (2023) (neq  $\Delta\text{TA}_{2400}$ , Gran Canaria) and Suitner et al. (2024) (neq  $\Delta\text{TA}_{2600}$~~   
195 ~~and  $\Delta\text{TA}_{2800}$ , Raunefjorden, also see section 2.1). Similar to the incubations from the Raunefjorden, the filters~~  
196 ~~from the Gran Canaria campaign originate from TA-gradient experiment, utilizing the local oligotrophic seawater~~  
197 ~~( $\text{TA}_{\text{initial}} \sim 2411 \mu\text{mol kg}^{-1}$ ,  $S \sim 36.6$ ,  $\text{pH} \sim 8.15$ ,  $T \sim 23^\circ\text{C}$ ) to test the stability of alkalization approaches (see SI for~~  
198 ~~further details).~~

199 **3 Results**

200 **3.1 Numerical logistic curve-fittings**

201 Three OAE gradient approaches by Suitner et al. (2024) were examined to test the stability of TA and to generate  
 202 refined numerical logistic curve fittings of the temporal development of TA and  $\Omega_{ar}$  (Figs. 3, S44 and S52). The  
 203 coefficients (b) and (c) (see Fig. 2) were determined by numerical interpolation to optimize the fit to Eq. (1) and  
 204 its derivative *in equal proportions*. Therefore, the shown functions were optimized to describe the temporal  
 205 evolution, while also including the rate loss changes, which allowed an improved description of the runaway  
 206 process in comparison to the approaches in previous studies. Outlying data points displaying an anomalous  
 207 increase or stagnation in values in the filtered approaches were removed from curve-fitting calculations (for  
 208 details see *section 3.2 and SI*). For each treatment, continuous differentiable functions to describe and analyze  
 209 the runaway carbonate precipitation process during OAE approaches were generated. To illustrate the described  
 210 processes and trends, the unfiltered neq approach was selected as an example (Fig. 3). The plots for the filtered  
 211 approaches are provided in the SI (Figs. S44, S52 and S63).  
 212

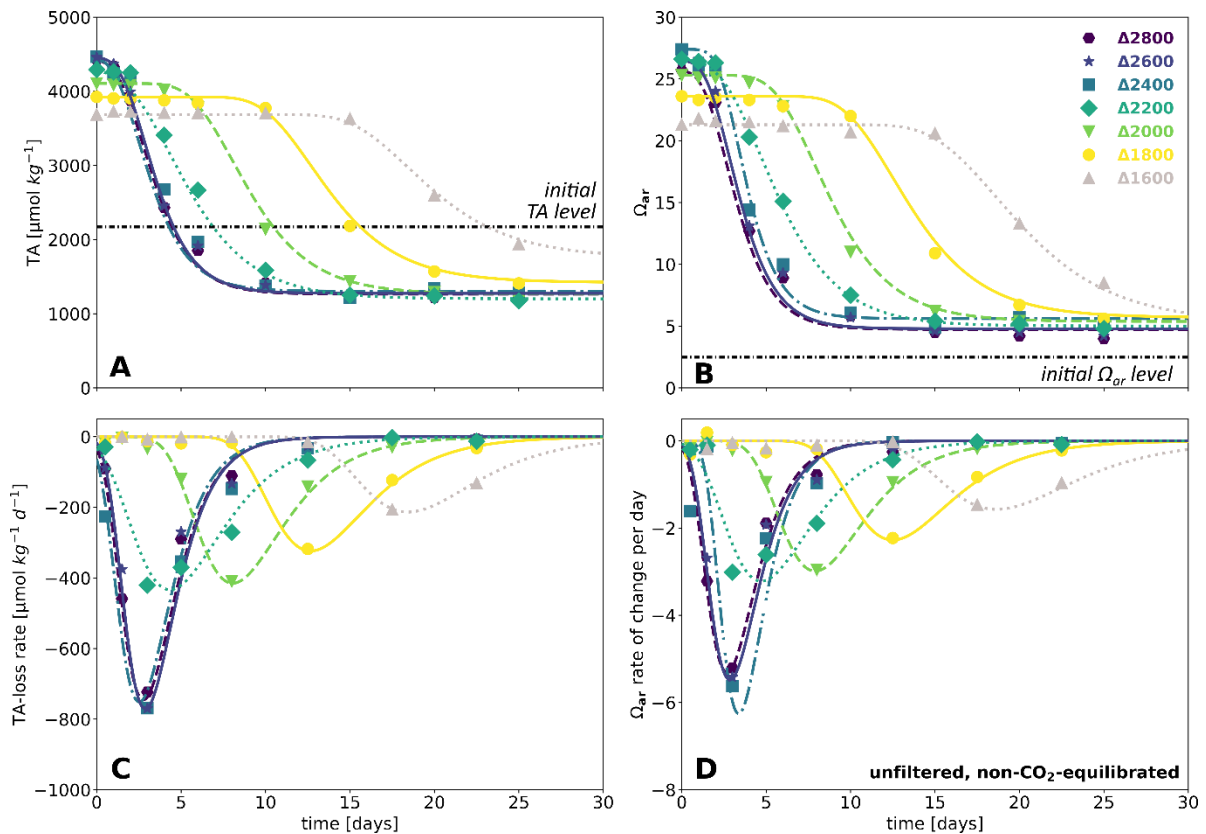


Figure 3: Results of the numerical curve fits – for the unfiltered neq approach, TA evolution over time (A),  $\Omega_{ar}$  evolution over time (B), TA-loss rate over time (C),  $\Omega_{ar}$  rate of change over time (D). Line plots: curve-fitted continuous functions, markers: measured data points, for related diagrams for filtered approaches see Figs. S44, S52 and S63.

213

214 For the unfiltered neq experiment (Fig. 3), treatment levels  $\Delta TA_{1600}$  and higher entered into an APP after  
 215 exceeding critical TA levels to initiate the runaway carbonate precipitation process. Treatments levels  $\Delta TA_{2400}$ -

216 <sup>2600</sup> exhibited a buffering as a consequence of magnesium hydroxide precipitation (see Badjatya et al., 2022;  
217 Ringham et al., 2024; Suitner et al., 2024; Varliero et al., 2024), which prevented an increase above  $\sim 4470 \mu\text{mol}$   
218  $\text{kg}^{-1}$  in TA and  $\sim 27.4$  in  $\Omega_{\text{ar}}$ . The buffering effects were not recognized within the fitting procedure and the first  
219 data point (after  $\sim 3$  min runtime) of each treatment level was set as the baseline.

220 The continuous logistic curve-fits allow the estimation of the APP onset and duration. Parameter (b) correlates  
221 with the induction time, while (c) correlates with the APP timespan (see Figs. 4 and 5). Under the present  
222 conditions the regressions can be used as conversion equations for TA evolution. Related conversions and  
223 regressions are provided in the SI (Fig. S7).

224

### 225 **3.2 Outliers**

226 In the experimental series performed in the Raunefjorden, a systematic cessation of the precipitation process  
227 was observed in two of the three experimental setups. Precipitation arrested after 6 days, in the eq filtered  
228 approach (Fig. S1) and after 8 days in the filtered neg approach (Fig. S2). For all TA treatments that had already  
229 entered the accelerated precipitation phase, no further significant changes were detected in any measured  
230 parameter.

231 Each TA treatment level was distributed to three individual bottles to minimize headspace effects while providing  
232 sufficient volume for sampling. The bottles were sampled sequentially three to four times each, after which a  
233 fresh set of bottles was opened. Although both affected series were run concurrently, a logistical offset of two  
234 days separated their start times. All anomalies in the two independent series occurred between June 24th and  
235 28th 2022, specifically in the second set of opened bottles, while the first and last sets of bottles displayed a  
236 regular precipitation pattern. This temporal clustering suggests that an external factor, such as water  
237 temperature, sunlight intensity, or a particular aspect of the sampling procedure, may have systematically  
238 influenced the affected reactor bottles. Repeated measurements with calibrated standards ruled out an  
239 analytical error, and the concurrent impact on both pH and TA confirms the reliability of the recorded values.  
240 Consequently, the two sampling days that exhibited these anomalies were excluded from the curve-fitting  
241 calculations. A comparison of the fits with and without these data points is shown in supplementary  
242 Figures S1, S2, and S3.

243

244

### 245 **3.3~~2~~ Induction time and timespan of the APP**

246 By employing the logistic curve fits, the temporal evolution of each approach could be parameterized. To identify  
247 the temporal stability ranges and reflect the transition from stable to precipitation-dominated system modes, a  
248 criterion of  $40 \mu\text{mol kg}^{-1} \text{d}^{-1}$  rate of change in TA was set. This rate provides a sufficiently high threshold to exclude  
249 a false detection due to natural variability or measurement errors, while still being low enough not to overlook  
250 a significant fraction of TA-loss (see Fig. S1~~54~~ for varying criteria).

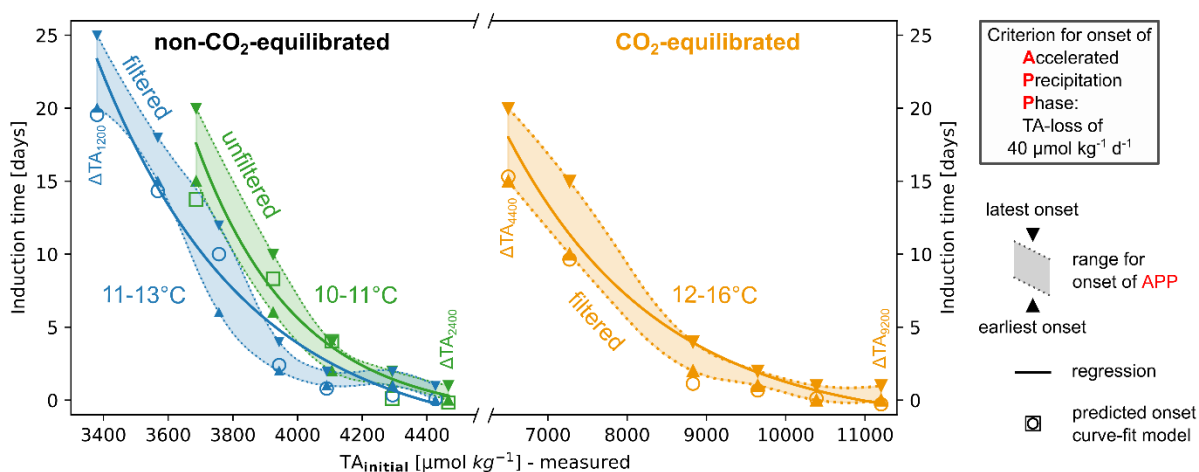
251 Based on this criterion, Fig. 4 illustrates the induction times for the APPs. The shaded ranges indicate  
252 extrapolated timeframes between subsequent measurements during which the initiation of the APP for each  
253 treatment was detected. The displayed regressions were calculated using the averaged times from two

254 consecutive measurement days. For comparison, hollow markers represent predictions from the presented  
 255 curve-fitted functions. The regressions of the induction times uniformly follow an inverse exponential trend of  
 256 the type:

$$t(TA) = f e^{-g TA} - h \quad (5)$$

257 The employed data series covered a range of 25 days with progressively increasing induction times from 0 to 20  
 258 days for treatments reaching  $\sim 4470$  ( $\Delta TA_{2400}$ ) to  $\sim 3380$   $\mu\text{mol kg}^{-1}$  ( $\Delta TA_{1200}$ ) in the filtered neq experiment and  
 259  $\sim 11200$  ( $\Delta TA_{9200}$ ) to  $\sim 6500$   $\mu\text{mol kg}^{-1}$  ( $\Delta TA_{4400}$ ) in the filtered eq experiment. Treatment levels above  $\Delta TA_{2400}$  in  
 260 the neq approaches exhibited an immediate onset of TA-loss due to the precipitation of secondary hydroxides  
 261 and/or carbonate minerals, therefore, following the presented criterion, practically leading to their immediate  
 262 entry into the APP process.

263 The same relationships and trends can also be applied using  $\Omega_{ar}$  as a variable. While the neq approaches exhibited  
 264 lower  $\Omega_{ar}$  values (17.8-27.4) compared to the eq treatments (19.5-43.6), the onset of the APP in the neq  
 265 experiments occurred significantly earlier. This indicates that  $\Omega_{ar}$  is not the only decisive factor guiding the  
 266 (pseudo-) homogeneous nucleation process, determining the induction time.



267 Figure 4: Induction time for the onset of APP in relation to the initial TA addition level, based on the first detection of a TA-loss  
 268 rate of  $40 \mu\text{mol kg}^{-1} \text{d}^{-1}$ . Each pair of triangle markers represents two consecutive measurement days during which the set loss  
 269 rate criterion was met; hollow markers: predicted induction times for each treatment level, based on the introduced curve-fit  
 270 model. Exponential regression of average experimentally detected induction time, see Eq. (5) in Tab. 2 for related functions.  
 271

272 Table 2: Regressions of induction times, see Fig. 4. Note that the use of the given equation should not be generalized, as it is  
 273 only valid under the presented environmental conditions. Also be aware that the resulting predictions of induction times far  
 274 out of the specified TA addition ranges might not be accurate.

$t(TA_{initial}) = f e^{-g TA_{initial}} - h \quad (5)$			Regression			
Treatment		Temp. [°C]	$f * 10^3$	$g * 10^{-4}$	h	$R^2$
non- equilibrated	unfiltered	10-11	2721.769	32.233	1.215	0.996
	filtered	11-13	39.633	21.646	2.972	0.977
equilibrated	filtered	12-16	0.603	5.243	1.934	0.988

275

276 **3.43 Timespan of the APP**

277 To describe the temporal evolution of TA and  $\Omega_{ar}$  during the observed runaway processes for the present setups,  
 278 coefficients **(a)** and **(d)** in Eq. (1) can be set, while **(b)** could be evaluated by empirical or modeled data.  
 279 Consequently, only the duration of the APP represented by **(c)** needs to be estimated to enable the entire model  
 280 description of the precipitation procedure. The discrete nature of sampling days with decreasing frequency of  
 281 samplings towards the end of an experiment (up to 5 days) did not allow reliable empirical determinations of **(c)**.  
 282 The displayed APP timespans in Fig. 5 were therefore determined by the predictions of the presented curve-fits  
 283 (Fig. 3), based on the  $40 \mu\text{mol kg}^{-1} \text{d}^{-1}$  TA-loss criterion to define the start and endpoint of the APPs. Fig. 5  
 284 illustrates the related predicted timespans against the initially reached TA levels, categorized by the individual  
 285 experimental setups. The neq APPs form distinct clusters for each approach, which again can be subdivided into  
 286 treatments with and without the occurrence of immediate precipitation. Regardless of the initial TA  
 287 enhancement level, treatments that exhibited an immediate decline due to  $\text{Mg}(\text{OH})_2$  formation showcased  
 288 almost identical APP spans (unfiltered  $\sim 8.8$  and filtered  $\sim 5.9$ - $7.4$  days) within each approach. Although the neq  
 289 treatments without  $\text{Mg}(\text{OH})_2$  had the same starting conditions, the unfiltered experiments exhibited  
 290 approximately 4 days longer APPs. In the eq approach, the APPs showed a continuous decrease as the initial TA  
 291 addition levels increased, ranging from 5 to 11 days.

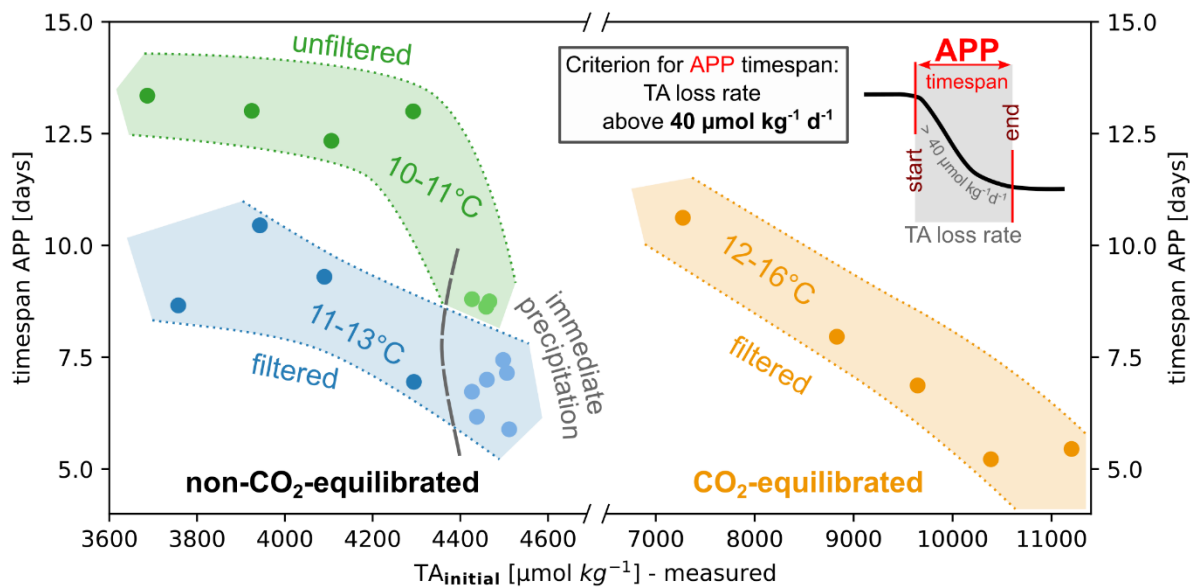


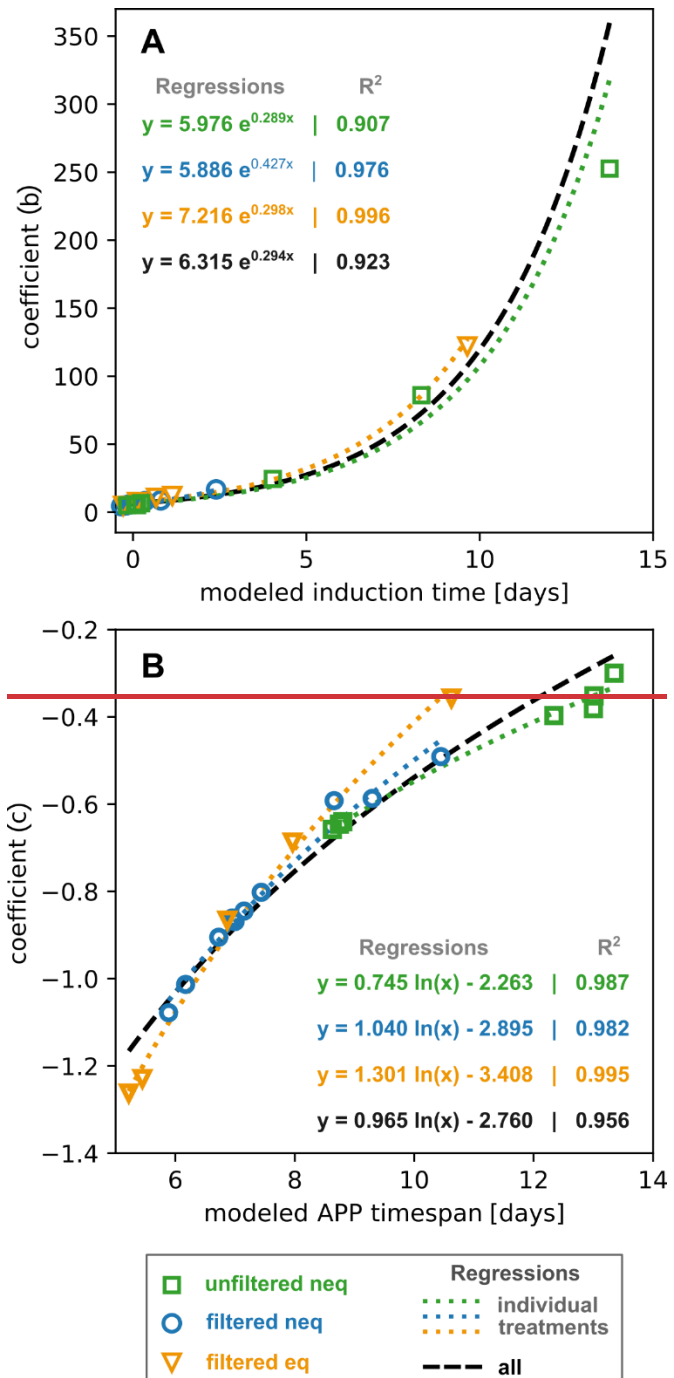
Figure 5: Overview timespans of APP in relation to the initial TA addition level; determined by the outcomes of the presented numerical logistic curve-fitting. Presented timespans are based on the introduced TA-loss criterion (see section 3.32), which was defined as period with rates above  $40 \mu\text{mol kg}^{-1} \text{d}^{-1}$ ; only treatments which reached the final stable stage were considered, neq treatments labeled with immediate precipitation showcased a loss of TA within the first 3 min of the experiment – most likely as a consequence of  $\text{Mg}(\text{OH})_2$  formation.

292

293 **3.4 Prediction of onset and timespan of APP**

294 The established continuous logistic functions allow estimations of effects occurring between measurement  
295 points, thereby improving the overall accuracy beyond what discrete experimental datasets could provide. Based  
296 on the  $40 \mu\text{mol kg}^{-1} \text{d}^{-1}$  TA loss criterion (see section 3.2 and sketch Fig. 5), these functions could therefore assess  
297 the initiation of the APP for specific initial TA and  $\Omega_{\text{calc}}$  levels, as well as a given starting particle surface area (see  
298 regressions in Fig. 4). In this regard, Fig. 6 illustrates the correlations of the curve fitted coefficients **(b)** and **(c)**  
299 and their related entities of the modeled induction times and APP timespans (see Fig. 2). Under the present  
300 physicochemical conditions, the provided regressions could be utilized as conversion equations to estimate the  
301 TA development of a treated water mass based on an existing database or to convert observational data into  
302 mathematically expressible equations for predicting the future evolution. Note that the high correlations of  
303 coefficients **(b)** and **(c)** with induction times and APP timespans are relate to the circumstance that both  
304 coefficients are determined through the described numerical curve fitting procedure, which is based on the  
305 properties of the logistic function and thus indirectly incorporates information about induction times and APP  
306 timespans.

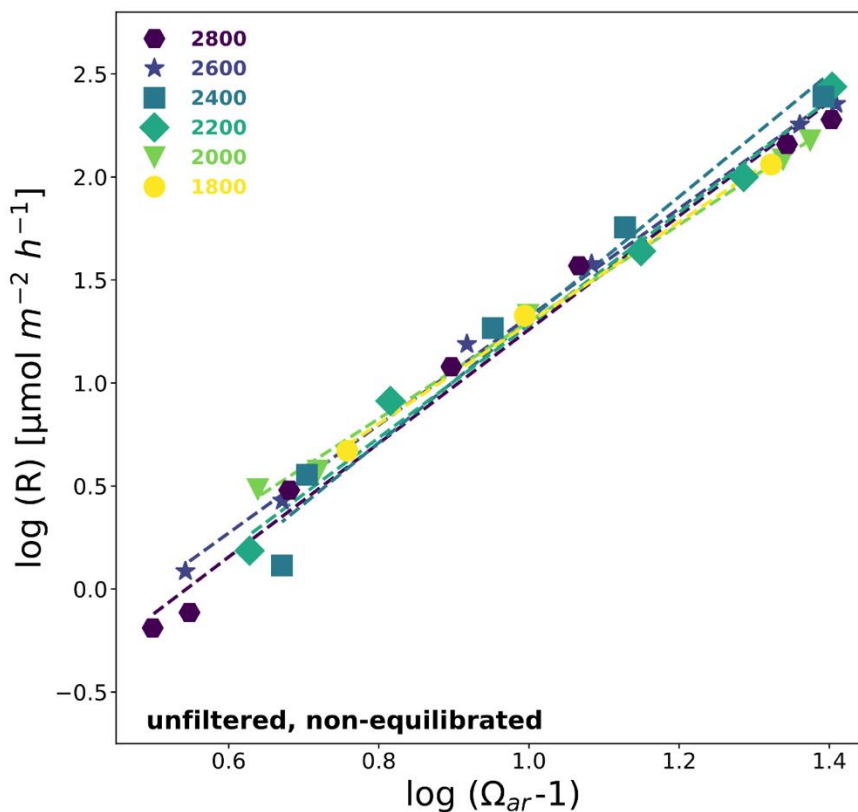
Figure 6: Regressions describing the relationships between the coefficient (b) and the modeled induction time [A], as well as the coefficient (c) and the modeled APP timespan [B] for each approach. The shown regressions allow for the conversion of specifiable time dependent characteristics of a runaway process to the coefficients of the presented inverse logistic function (Eq. (1)). Specified relationships should not be generalized and are only valid within the given conditions of each approach.



### 307 3.5 Empirical rate equations

308 Additional insights into the reaction speed and the associated timespan of the APP can be obtained through  
 309 analysis of empirical rate law equations. As an example, Fig. 67 illustrates the relationship between the logarithm  
 310 of TA-loss rates normalized to the surface area and the aragonite saturation states for the unfiltered neq  
 311 approach (see Figs. S84 and S95 for details on the filtered approaches), focusing on treatments that entered the  
 312 APP. Throughout all experiments the logarithm of the surface area normalized TA-loss/precipitation rates R  
 313 correlates with the  $\log(\Omega_{ar}-1)$ , in accordance with similar observations reported in literature (e.g. Morse et al.,  
 314 2007; Mucci & Morse, 1983; Zhong & Mucci, 1989). The parameters n and k in Eq (2)  $R = k(\Omega_{ar}-1)^n$  were  
 315 determined for each treatment level in this work, as outlined in Eq (2) to (4) (section 2.3). Here, R represents the  
 316 surface area normalized precipitation rate, TA-loss rate, and k denotes the rate constant.

317 The values for  $n$  and  $\log(k)$  derived from the linear regressions in the unfiltered neq treatments are provided in  
 318 Tab. 3 (see Tabs. S64 and S75 for filtered experiments). These values demonstrate reasonable consistency in  $n$   
 319 and  $\log(k)$  within each of the three separate experiments. Treatment levels influenced by the immediate  
 320 formation of  $\text{Mg}(\text{OH})_2$  as pH approached approximately 10.3 show minor deviations, the remaining treatment  
 321 levels exhibit reaction orders ( $n$ ) within a relatively narrow range of 2.45 to 2.73. In comparison,  $\log(k)$  values  
 322 ranged between 0.30-1.68, showcasing a higher variability.



323 *Figure 67: Carbonate precipitation kinetics for unfiltered neq treatments that entered the APP; see Tab. 3 for related*  
 324 *regressions and rate equations.*

325 Table 3: Overview of coefficients and regressions of empirical rate equations for unfiltered neq treatments, also see Fig. 67  
 326 and Tab. S86 for cross-comparison of all treatments.

Treatment	$\log(R) = n(\Omega_{ar} - 1) + \log(k)$			
$\Delta TA$	n	$\log(k)$	$R^2$	$\hat{\sigma}$
<b>2800</b>	2.76	-1.50	0.989	0.117
<b>2600</b>	2.62	-1.30	0.997	0.055
<b>2400</b>	2.98	-1.68	0.975	0.167
<b>2200</b>	2.73	-1.45	0.989	0.106
<b>2000</b>	2.35	-1.06	0.997	0.046
<b>1800</b>	2.45	-1.16	0.996	0.060
<b>all</b>	2.68	-1.39	0.985	0.106

327

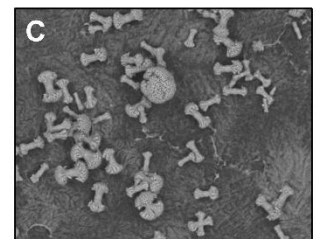
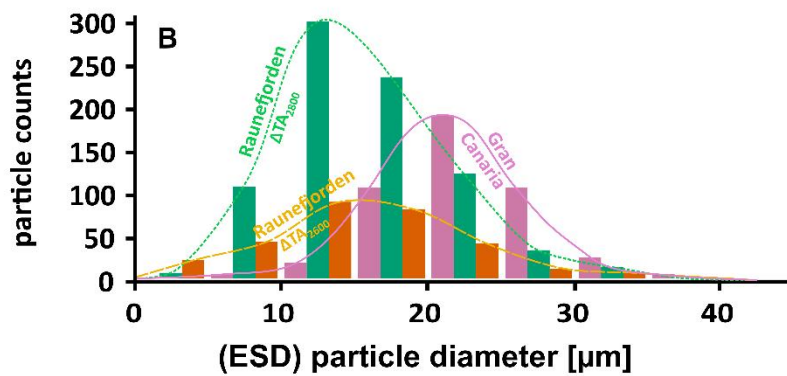
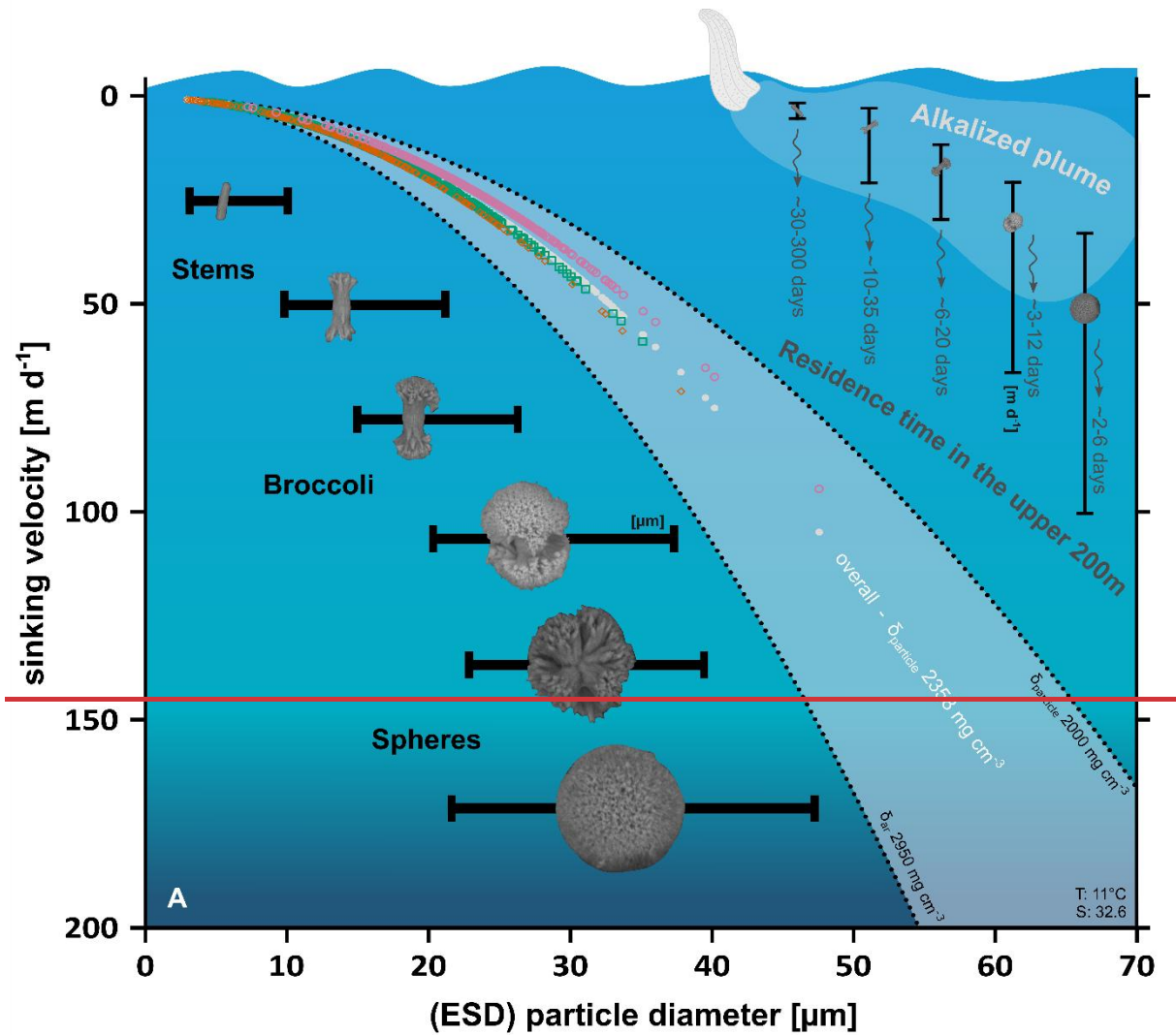
### 328 3.6 Evolution of particles and sinking speed

329 To assess the impact of secondary precipitated particles during OAE approaches, precipitated materials from the  
 330 studies by Hartmann et al. (2023) and Suitner et al. (2024) were analyzed for shape, size, and sinking velocity. As  
 331 qualitatively depicted in these studies, the aragonite precipitates manifest and evolve in a variety of forms and  
 332 sizes, ranging from stem-like structures, followed by double-broccoli shapes and ultimately forming closed  
 333 spheres (see Fig. 78).

334 For this study the length and width distribution of 950 precipitated particles were determined by manual  
 335 inspection of four overview SEM images (see Fig. S117) from Gran Canaria samples (see Hartmann et al., 2023  
 336 for details; analyzed treatment level:  $\Delta TA_{2400}$ , filtered, neq, Temp.  $\sim 23^\circ C$ , Sal.  $\sim 36.5$ , runtime 4 days) and the  
 337 Raunefjorden, Bergen (this study and Suitner et al., 2024, see Figs. 3 and 7 therein; analyzed treatment levels:  
 338  $\Delta TA_{2800}$  and  $\Delta TA_{2600}$ , Temp.  $\sim 11^\circ C$ , Sal. 32.6, runtime 25 days – highest unfiltered neq treatments). Results of this  
 339 evaluation are provided in Fig. S128. Length and width distributions of the formed particles follow distinct ratios,  
 340 allowing the definition of three categories: **1.** Stems ( $<0.5$ ), **2.** Broccoli ( $0.5 < x < 0.9$ ) and **3.** Spheres ( $>0.9$ ). Note  
 341 that this method also categorizes regularly shaped, multi-branched particles as spheres (see Fig. 78). Precipitates  
 342 from the Gran Canarian campaign primarily comprised well-developed broccoli and spherical-shaped particles,  
 343 whereas the samples from the Raunefjorden were characterized by less evolved stems and broccoli as the  
 344 dominant components. Although the runtime for the Gran Canarian sample was considerably shorter (4 days) in  
 345 comparison to the Raunefjorden (25 days), the  $\sim 12^\circ C$  difference in temperature led to significantly higher  
 346 precipitation rates and more developed shapes. The analyzed Raunefjorden samples originate from the same  
 347 experiment and differ only in the initially added TA-level of  $200 \mu mol kg^{-1}$ . Even this minor difference in TA  
 348 addition resulted in the presence of more evolved shapes in the higher treatment.

349 The gravitational sinking velocities of precipitated particles were measured using a FlowCam setup (see Bach et  
 350 al., 2012 for technical details). Based on the concept of equivalent spherical diameters (ESD) the density of each  
 351 particle was calculated, revealing a range from  $1.54$  to  $3.18 g cm^{-3}$  for ESD sizes between  $12$  and  $50 \mu m$ . The  
 352 average density was determined to be  $2.358 g cm^{-3}$ . The discrepancy with the density of aragonite ( $\sim 2.95 g cm^{-3}$ )

353 may result from an overestimation of particle sizes in the calculation method, which relies on an inversion of  
354 Stokes' Law for the terminal sinking velocity of perfect spheres. However, most particles are non-spherical and  
355 contain numerous internal cavities within their structure (see Fig. S7), and their densities are therefore expected  
356 to be lower than those of pure aragonite. The determined particle density was then used to calculate the  
357 theoretical sinking velocities of the manually counted precipitated particles. To account for potential variability  
358 in particle density, Fig. [78](#) presents a range of sinking velocities of the counted precipitates.  
359 Measured sinking velocities for precipitated particles within the aforementioned density range varied from  $\sim 5$  m  
360  $d^{-1}$  (14  $\mu m$  particle) to  $\sim 47$  m  $d^{-1}$  (41  $\mu m$  particle). Recorded particles in the ESD range of 50-180  $\mu m$  were not  
361 included in the calculations, as they were not observed within the same filter material that was analyzed by visual  
362 inspection. Discrepancies between measured and calculated values may reflect aggregation effects or technical  
363 limitations of the utilized FlowCam to track particles smaller than 3  $\mu m$  (Bach et al., 2012).  
364 Derived from the calculated sinking velocities, the residence times within the upper 200 m of the water column  
365 were determined. Accordingly, under idealized conditions, early precipitated stages, such as stems ( $<10\mu m$ ),  
366 could remain for a few months within the upper ocean layer, providing potential additional surfaces for an  
367 ongoing heterogeneous precipitation if a continuous local alkalization is applied. In contrast, precipitates  $>30$   
368  $\mu m$  would descend within days to deeper ocean layers, not affecting the precipitation behavior of continuous  
369 surface alkalization attempts. Notice that sinking velocities are temperature and salinity dependent, and  
370 therefore would vary under different environmental conditions (see Fig. [S139](#)).



Example SEM filter of carbonate precipitates and their variety of shapes (for further details see Fig. S1)

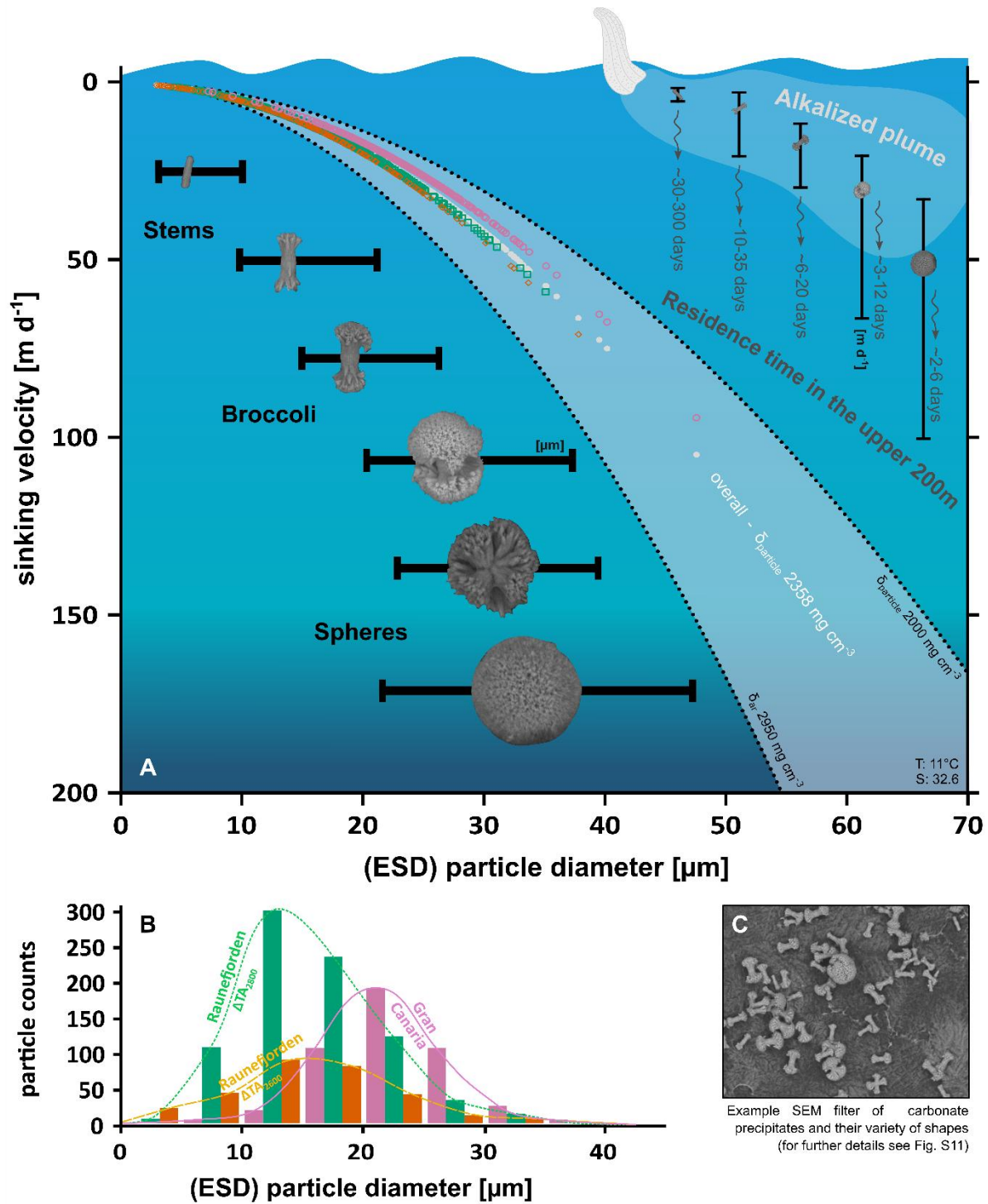


Figure 79: (A) Calculated sinking velocities of particles (hollow markers) as a function of ESD for each treatment (green squares: neq unfiltered  $\Delta\text{TA}_{2800}$  – Raunefjorden, Bergen; orange diamonds: neq unfiltered  $\Delta\text{TA}_{2600}$  Raunefjorden, Bergen; pink circles: neq filtered  $\Delta\text{TA}_{2400}$  Gran Canaria). ESD distribution of stem, broccoli and sphere shaped precipitates (horizontal) and their calculated mean residence time in the mixed layer (assumed to be 200 m), while neglecting particle growth processes (B) related particles counts in size fractions of 5  $\mu\text{m}$ , also see Fig. S812 for length:width distribution (C) example section of a SEM filter ( $\Delta\text{TA}_{2600}$  Raunefjorden), see Fig. S117 for complete set of all filters.

## 372 4 Discussion

### 373 4.1 General findings

374 By analyzing the experimental datasets provided by Suitner et al. (2024), this study demonstrates that the  
375 process of TA-loss during runaway carbonate precipitation follows quantifiable relationships. For the present  
376 study, the compiled concepts allowed the description of the principles guiding the entire runaway process. The  
377 obtained capability to predict TA-stability ranges, in terms of time and magnitude, might help prevent secondary  
378 mineral formation, thereby optimizing the assessments for OAE application scenarios. Furthermore, the  
379 simplicity of the logistic curve fit model, along with the demonstration that the carbonate precipitation follows  
380 simple rate law equations (see Morse et al., 2007; Mucci & Morse, 1983; Zhong & Mucci, 1989), might facilitate  
381 the straightforward integration of these fundamental mechanisms into ocean models like the studies by He &  
382 Tyka (2023), Ou et al. (2025), Schwinger et al. (2024), Wang et al. (2022) or Zhou et al. (2024). The relationships  
383 reported herein are specific to the experimental setup and the particular environmental conditions under which  
384 they were measured. Consequently, projections or models that apply the presented precipitation patterns and  
385 equations may not hold when conditions differ from those of the original study.

### 387 4.2 Nucleation and onset of accelerated precipitation phase

388 Previous studies examining the evolution of the runaway precipitation process in the context of OAE (Hartmann  
389 et al., 2023; Moras et al., 2022, 2024; Suitner et al., 2024) observed and described considerable periods with  
390 stable TA levels before the onset of the APP (see Fig. 1), depending on the TA and DIC levels.

391 In theory, even at natural background supersaturation levels in the ocean, (pseudo-)homogeneous precipitation  
392 is expected to occur at very slow rates, on timescales of thousands of years (Pytkowicz, 1965, 1973). Regardless,  
393 the nucleation and precipitation processes in ocean waters are suppressed by inhibitory species like  $Mg^{2+}$   
394 (Berner, 1975; Pan et al., 2021; Pokrovsky, 1998), phosphate- (Burton & Walter, 1990) or dissolved organic  
395 matter (Chave & Suess, 1970; Kellock et al., 2022; Moras et al., 2024). Naturally occurring precipitation events in  
396 the ocean are associated with sporadic unique-occurrences such as flash floods (Wurgaft et al., 2016, 2021) or  
397 observed during whiting events (Broecker & Takahashi, 1966; Bustos-Serrano et al., 2009; Morse et al., 2003),  
398 providing high degrees of (re)suspended sediments that catalyze a heterogeneous carbonate precipitation  
399 procedure.

400 To consider the persistent (pseudo-)homogeneous precipitation within typical natural seawater supersaturation  
401 ranges, the terminology concerning specific stability ranges of TA or timeframes for the onset of secondary  
402 carbonate formation should be refined. However, within typical observation times in the Earth system, the  
403 precipitation of secondary calcium carbonate in particle-free seawater solutions is expected to be suppressed to  
404  $\Omega_{ar}$  values of approximately 11.3 or below (derived from Eq. (4) in Marion et al. (2009), based on data by Morse  
405 & He (1993) and Morse et al. (2007)).

406 Nevertheless, even a 0.2 $\mu$ m-filtered natural seawater contains around  $\sim 10^9$  particles per ml in the size range of  
407 5-120 nm, already offering a total surface area of around 8 m<sup>2</sup> per m<sup>3</sup> (cf. Wells & Goldberg, 1992), potentially

408 acting as a catalyst to initiate carbonate precipitation in alkalinity treated seawater. In the presence of surfaces  
409 for pseudo-homogeneous/ heterogeneous precipitation such as suspended sediments, colloids, organic matter  
410 or the introduced solid alkalization substrates, Moras et al. (2022) reported an  $\Omega_{ar}$  threshold of  $\sim 5-7$  for the  
411 observable onset of carbonate formation for the given runtime of the experiment. Potentially, the colloidal  
412 structure of  $Mg(OH)_2$  precipitates (see Badjatya et al., 2022), typically formed above pH values of  $\sim 10.5$  as a  
413 consequence of TA addition (cf. Eisaman et al., 2023; Haas, 1916; Kapp, 1928; Suitner et al., 2024; Varliero et al.,  
414 2024) could serve the same purpose and lower the threshold for carbonate precipitation. However, the  
415 redissolution of the formed  $Mg(OH)_2$  through the mixing and dilution processes, as described by Ringham et al.  
416 (2024), may inhibit this effect and would also allow much higher short-term pH and TA concentrations around  
417 an alkalinity injection site when using liquid stock solutions.

418 To characterize the transition from a state with negligible shifts in carbonate chemistry towards a phase primarily  
419 driven by carbonate formation, a practicable criterion of a  $40 \mu\text{mol kg}^{-1} \text{d}^{-1}$  TA-loss was set to determine the start  
420 of the intensified precipitation stage (see Figs. 4 and 5). This criterion was also used to describe the induction  
421 time, which is the period before a measurable onset of secondary carbonate formation can be detected (Fig. 4).  
422 Since the induction time includes a fundamental uncertainty, it does not reflect an intrinsic property of the  
423 treated solution itself and relies on the detection capability of the experimental setup (Söhnel & Mullin, 1988)  
424 and might be chosen differently in future work (see Fig. S15~~4~~ for varying criteria). While the selected criterion  
425 already depicts relatively high loss rates, it enables detectable changes, distinguishable from measurement  
426 uncertainties or natural variabilities. The overall emerging patterns related to the onset and duration of the APP  
427 nevertheless remained relatively consistent across different tested threshold values.

428

#### 429 **4.3 Predictability of the runaway process**

430 The consistent patterns during the TA-loss within all three experimental setups allowed the introduction of  
431 continuous and differentiable functions for each treatment level, enabling further analysis to examine relevant  
432 factors guiding the runaway process. Fuhr et al. (2022) utilized a comparable inverted logistic function to model  
433 the process of secondary carbonate formation during olivine dissolution experiments in seawater. However, the  
434 model was not consistently applied to describe a runaway carbonate precipitation process nor used as a general  
435 predictive model to determine the stability ranges of the added TA in OAE approaches.

436 The characteristics of the logistic function applied in this study, facilitate the conversion of both empirically  
437 determined and hypothetical parameters, such as induction time, duration of the APP (Fig. 5), or the initial and  
438 final TA levels before and after the runaway process. The applicability of kinetic rate equations, combined with  
439 the ability to quantify the precipitation process, enables a description and prediction of the temporal evolution  
440 of the carbonate formation. This may facilitate the integration of the TA depletion procedure into various  
441 predictive modeling approaches. Although these statements currently apply only under the tested  
442 environmental conditions, they nonetheless suggest the general capability to assess a framework for guiding  
443 time and TA level ranges in OAE approaches. Since the logistic model is based on experimental data from bottle  
444 experiments, processes such as the removal of surface area due to the sinking of precipitated carbonate particles  
445 were not accounted for. See section 4.6 for an approach to address this topic.

446 Under specified temperature and salinity conditions, as well as predefined TA/DIC levels after OAE treatment  
447 and an estimated final  $\Omega_{ar}$  after the precipitation process stopped (typically  $\sim 1.5$ - $5.0$ , see Fuhr et al., 2022;  
448 Hartmann et al., 2023; Moras et al., 2022; Pan et al., 2021; Suitner et al., 2024), the resulting total TA-loss can be  
449 computed. This calculation follows the condition that the TA-loss reflects the ideal 2:1 TA:DIC ratio during  
450 carbonate mineral precipitation in seawater (Zeebe & Wolf-Gladrow, 2001). Given these assumptions, upper and  
451 lower limits of the logistic function (coefficients **(a)** and **(d)**, Eq. (1)) can be determined. To characterize measures  
452 such as induction time (coefficient **(b)**) and the duration of the APP (coefficient **(c)**), it is necessary to acquire  
453 empirical data that account for the specific conditions of the deployment area. These data could either be  
454 provided by actual experiments or model predictions, based on a comprehensive database which accounts for  
455 broad ranges of TA, DIC, temperature, salinity, and practical available surface area, as well as inhibitory factors  
456 or potential effects of biota. To validate the predicted precipitation behavior, additional gradient experiments  
457 need to be conducted to better understand the geochemical reaction pathways.

458

#### 459 **4.4 Empirical rate equations using $\Omega_{ar}$ and particle surface area during APP**

460 After passing the induction time to start the detectable carbonate formation process by (pseudo-/)homogeneous  
461 precipitation and overcoming the delaying inhibition effects (Marion et al., 2009; Morse & He, 1993; Schulz et  
462 al., 2023), the triggered heterogeneous precipitation can be described by basic empirical rate equations (Fig. [67](#),  
463 [S84](#) and [S95](#)). These equations demonstrate the fundamental role of  $\Omega_{ar}$  as a guiding factor for the precipitation  
464 process. The kinetics of carbonate formation remained relatively consistent across all treatment levels within  
465 each experimental approach (see Tabs. 3, [S64](#) and [S75](#)). The observed consistent correlations between saturation  
466 states and surface area normalized precipitation rates indicate that the runaway carbonate formation processes  
467 during the present incubations followed the known kinetics of heterogeneous carbonate formation in seawater  
468 (cf. Morse et al., 2007; Zhong & Mucci, 1989).

469 Fig. [89](#) illustrates the role of  $\Omega_{ar}$  saturation states and generated particle surface area in guiding the TA-loss rates  
470 during the precipitation process. The black line represents the curve fit of TA-loss rates of the unfiltered neq  
471  $\Delta TA_{2000}$  approach; the experimentally determined rates are indicated by black triangles (also see Fig. 3c).  
472 Assuming that the entire lost TA was transformed into aragonite precipitates with a surface area of  $2.283 \text{ m}^2 \text{ g}^{-1}$   
473 (see section 2.3), the total generated particle surface area (PSA) could be determined (red, dash-dotted line).  
474 The overall expected TA-loss rate per  $\text{m}^2$  (brown, dashed line) was obtained by utilizing the empirical logistic  
475 curve fit for the temporal evolution of  $\Omega_{ar}$  (Fig. 3b), normalizing it to  $1 \text{ m}^2$  surface area, and inserting it into the  
476 rate equation (Eq. (4)). Given that the system initially exhibits a negligible degree of PSA, the relatively high  
477 precipitation potential by the  $\Omega_{ar}$  saturation state does not result in a measurable TA-loss rate. Following the  
478 presented concept, the consistently high  $\Omega_{ar}$  values led to a continuous (pseudo-/)homogeneous precipitation  
479 during the induction time, thus causing a rise in PSA until the system shifts to heterogeneous precipitation, and  
480 ultimately resulting in a detectable exponential runaway process. The interplay of precipitation potential by  $\Omega_{ar}$   
481 and the practical available surface area could therefore be determined as the primary factors guiding the actual  
482 observed TA-loss rates.

483 Within the uncertainties of the applied calculation steps and methods, the practical TA-loss rate could simply be  
 484 described as the product of these two factors. To visualize this relationship, the dotted light blue line in Fig. 89  
 485 represents an empirical rate law equation that combines the shown PSA (red, dash-dotted line) and the surface  
 486 normalized expected precipitation rate (brown, dashed line) with the determined rate constant (k) and reaction  
 487 order (n) for the  $\Delta TA_{2000}$  treatment (see Tab. 3). The shape of the resulting function traces the measured TA-loss  
 488 rates (black triangles) within reasonable accuracy (see Fig. S140 for other treatments). Be aware that any kind of  
 489 inhibition effect is incorporated in the underlying experimentally determined temporal TA evolution, which  
 490 represents the basis for all shown parameters.

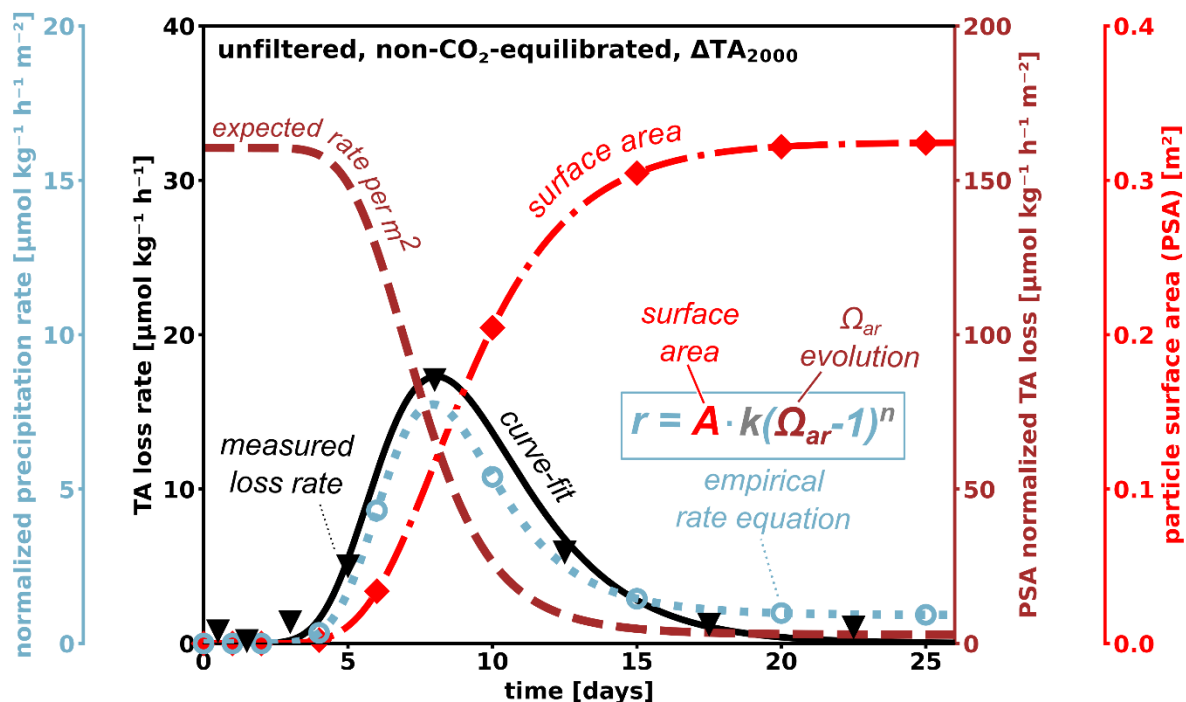


Figure 89: Conceptual figure, illustrating the interplay of  $\Omega_{ar}$  and particle surface area guiding the TA-loss rate evolution (dashed, brown). After TA injection high  $\Omega_{ar}$  values provide a high potential for the formation of carbonates by heterogeneous precipitation. In the absence of existing particle surface area (red dash-dotted), (pseudo-)homogenous precipitation would dominate the period until the start of the APP and the resulting runaway precipitation process. Observed TA-loss rates (black triangles) are therefore a combination of the available practical surface area and the precipitation potential by  $\Omega_{ar}$  oversaturation. The related empirical rate equation (dotted, light blue) connects these two factors with the determined rate constant (k) and reaction order (n), tracing the shape and symmetry of the measured TA-loss rate. Hollow light-blue markers provide the output of the related empirical rate equations for each sampling day. While the potential to precipitate carbonates decreases with progressive precipitation, additional surface area is generated. Understanding how long particles remain in a critical zone to maintain a full-grown runaway process is therefore relevant for future considerations. The shown TA and loss rate data are taken from the empirical data sets for the neq unfiltered  $\Delta TA_{2000}$  approach, see Fig. S140 for other treatments levels.

491  
 492 **4.5 Could a runaway process be triggered in an open world context?**  
 493 Mixing with untreated water around an injection point may lead to an efficient dilution below non-critical TA  
 494 levels within seconds to minutes. Such a process would effectively prevent TA leakage, as described in this study,  
 495 which assumes that the formed particles act as catalysts for future precipitation. This is supported by findings

496 from a mesocosm experiment and corresponding side experiments, [wherein which](#) the presence of additional  
497 suspended aragonite particles accelerated ~~the~~TA-loss (Paul et al., 2024). In contrast, fresh seawater enhanced to  
498 the same TA-levels did not show any TA-loss within 10 days in their experiments. These observations ~~indicate~~  
499 ~~suggest~~ that free-floating particles in the water column can accelerate heterogeneous precipitation in a runaway  
500 style.

501 Precipitation events can be triggered naturally without additional treatment, especially for locations with already  
502 relatively high  $\Omega_{ar}$  background levels, for example, due to high evaporation rates (Bialik et al., 2022) or high  
503 degrees of (re)suspended sediments present on carbonate platforms (Broecker & Takahashi, 1966; Bustos-  
504 Serrano et al., 2009; Morse et al., 2003), or close to river mouths (Wurgaft et al., 2016, 2021) providing additional  
505 PSA to catalyze precipitation events. Under inappropriate TA deployment circumstances, secondary mineral  
506 formation might be triggered locally around injection sites, within short timescales. Moras et al. (2022) suggested  
507 that visible APP starts around  $\Omega_{ar}$  of 5, ~~In the mostly particle-free waters of the Raunefjorden, this translates to~~  
508 ~~a which translates for the mostly particle-free water of the Raunefjorden into~~  $\Delta TA$  of  $\sim 245 \mu\text{mol kg}^{-1}$  ~~and~~  $\sim 580$   
509  ~~$\mu\text{mol kg}^{-1}$  applying during a neq and eq OAE approaches, respectively and~~  $\Delta TA \sim 580 \mu\text{mol kg}^{-1}$  ~~for an eq OAE~~  
510 ~~approach~~. The induction time before the APP begins can be estimated using Equation (5), based on the specified  
511 TA-loss criterion of  $40 \mu\text{mol kg}^{-1} \text{d}^{-1}$ . For the ~~mentioned~~ ~~equilibrium~~ configurations, the projected induction  
512 times would be 1074 days and 143 days, respectively. However, the predicted induction times lie far outside the  
513 calibration ranges specified in this study and may therefore be inaccurate. ~~Nevertheless,~~ since these projected  
514 APP induction times [fall within the suggested residence times of treated water in the upper ocean layers, it is](#)  
515 [necessary to conduct studies lasting at least as long as the projected timespans, depending on local](#) ~~are also within~~  
516 ~~the suggested residence times of treated water in the upper ocean layers, it is necessary to conduct studies~~  
517 ~~lasting at least for the projected timespans, depending on the local~~ environmental conditions.

518 Significantly shorter induction times were identified for subtropical conditions (Temp.  $\sim 23^\circ\text{C}$ , Sal.  $\sim 36$  psu, TA  
519  $\sim 2400 \mu\text{mol kg}^{-1}$ ). Hartmann et al. (2023) described an onset of the precipitation after just 4 days for a  $50 \mu\text{m}$   
520 filtered neq incubation with initial values of  $1050 \mu\text{mol kg}^{-1}$  for  $\Delta TA$  and  $\sim 15$  for  $\Omega_{ar}$ . Within the same setting,  
521 Paul et al. (2024) observed aragonite formation for a  $\text{CO}_2$  equilibrated setup with  $\Delta TA \sim 2300 \mu\text{mol kg}^{-1}$  and  $\Omega_{ar}$   
522  $9.74 \pm 0.15$  in mesocosms after 21 days.

523 ~~The upper end members of TA perturbations examined in this study (neq:  $\Delta TA > 2400 \mu\text{mol kg}^{-1}$ ; eq:  $\Delta TA > 9000$~~   
524  ~~$\mu\text{mol kg}^{-1}$ ) are not intended to represent realistic target background values for permanent open-world scenarios,~~  
525 ~~as such values would need to remain biologically compatible over the long term. Rather, they represent short-~~  
526 ~~lived, near-field conditions that may occur close to an injection site or in enclosed environments where dilution~~  
527 ~~with untreated water is limited. The gradient approach used here therefore served as a controlled experimental~~  
528 ~~framework to investigate the principles of secondary carbonate formation under extreme conditions. Although~~  
529 ~~these small-scale incubations cannot fully reproduce natural systems, they provide a useful means to study the~~  
530 ~~underlying processes in a well-defined setting.~~

531  
532 ~~The upper end members of TA perturbations presented in this study (neq:  $\Delta TA > 2400 \mu\text{mol kg}^{-1}$ ; eq:  $\Delta TA > 9000$~~   
533  ~~$\mu\text{mol kg}^{-1}$ ) are not expected to represent realizable target background values for permanent open-world~~  
534 ~~scenarios, which would likely be aligned with biological compatibility. High perturbations would just occur within~~

535 ~~short timeframes in the near field of an injection site or within enclosed environments without sufficient~~  
536 ~~potential for dilution with untreated water. The implemented gradient approach allowed to examine the~~  
537 ~~principles of secondary carbonate formation under controlled conditions. While such small-scale incubations~~  
538 ~~provide only a limited analogue for natural systems, they nonetheless permit the investigation of fundamental~~  
539 ~~processes in a well-controlled setup.~~

#### 541 **4.6 Consequence of sinking particles removing surface area for carbonate formation**

542 Because the TA-loss rate is proportional to the surface area of particles (Eq. (4)), removal of particles due to  
543 sinking processes or dilution with untreated water would result in slower precipitation rates. Small, formed  
544 particles may remain in the upper layer for several months (Fig. 78), while medium-sized particles may leave the  
545 treated water within a couple of days, depending on temperature and salinity conditions (Figs. 78 and S139).  
546 Particles larger than 15  $\mu\text{m}$  are expected to sink within one day under the environmental conditions of the  
547 Raunefjorden. If those particles were removed by sinking while they were still growing, it can be estimated that  
548 approximately 30-40% of the available surface area would be removed from the upper 10 m of the water column  
549 within one day (also see SI). This would decrease the precipitation rate accordingly as surface area and formation  
550 rates are linearly proportional. In a natural open ocean environment, the formation and sinking of precipitates  
551 are likely to interact with the existing background of organic and inorganic particles. While any type of particles  
552 could potentially serve as nucleation sites, aggregation would increase the sinking speed. These processes were  
553 not included in the current model calculations but may be relevant under different conditions. In general, the  
554 abundance and sinking of particles need to be addressed if the stability or loss of is to be assessed with a high  
555 level of confidence.

556 Efficient dilution of the treated water parcels could therefore significantly reduce ongoing precipitation,  
557 especially if the onset of the APP is initiated within the first few seconds. For example, this could be the case in  
558 the wake of a ship, in OAE applications utilizing existing marine traffic to distribute TA throughout the world's  
559 oceans (Caserini et al., 2021). ~~However,~~ particle-based alkalization approaches would nevertheless  
560 temporarily introduce additional surface area until its complete dissolution, and may cause the shift into the APP  
561 (Hartmann et al., 2023).

#### 562 **5 Conclusion**

563 TA leakage due to oversaturation sets a limit to the efficiency of OAE approaches. So far, the drivers of the  
564 process could not be quantified, preventing the implementation of TA-loss terms in applicability assessments for  
565 OAE. An induced runaway process follows predictable patterns that can be modeled using available surface area  
566 and aragonite oversaturation, identified as the main factors for the given environmental settings.

567 However, it is expected that parameterizations will systematically change along temperature and salinity  
568 gradients, as well as with naturally occurring variations in particle abundance and quality. The determination of  
569 their impact was not within the scope of this work; instead, this study aimed to provide a framework for how  
570 such needed parameterization can be achieved. Achieving a predictability of the induced TA-loss on a global scale  
571 would allow the identification of suitable locations for OAE or optimizing applications. Therefore, further

572 research across salinity and temperature gradients would also enhance the predictive capabilities of ocean  
573 models. Runaway TA-loss processes, as described in this study, would be significantly altered under natural  
574 conditions by dilution and particle export processes. If sinking of particles and dilution with untreated water are  
575 considered, the limitations of laboratory bottle experiments become evident. Nevertheless, they contribute  
576 valuable parameterizations for model development. Field experiments are necessary to evaluate the validity of  
577 the presented theoretical model framework with respect to dilution and particle sinking processes.  
578

579 **Data availability**

580 All datasets will be made available at the time of publication.

581 **Author contributions**

582 The idea for this work was conceived by NS, with contributions by JH and SV. NS, SV and PS performed the surface  
583 area- and sinking velocity/density measurements. NS interpreted the data with help from all co-authors. NS and  
584 JH wrote the text with contributions from all co-authors.

585 **Acknowledgements**

586 Peggy Bartsch (UHH), Carl Lim (UHH) and Julieta Schneider (GEOMAR) are thanked for supporting the preparation  
587 and execution of the experiments.

588 **Financial support**

589 This research has been supported by the German Federal Ministry of Education and Research through the  
590 CDRmare projects RETAKE-1: grant no. 03F0895F and RETAKE-2: grant no. 03F0965F; Horizon 2020 (OceanNETs;  
591 grant no. 869357); the Deutsche Forschungsgemeinschaft (grant no. 390683824), under Germany's Excellence  
592 Strategy (EXC 2037, "CLICCS"; grant no. 390683824) contribution to the Center for Earth System Research and  
593 Sustainability (CEN) of the University of Hamburg, as well as the Ocean Alk-Align project funded by the Carbon  
594 to Sea Initiative.

595 **Competing interests**

596 JHA is consulting the Planeteers GmbH. The contact authors have declared that all other authors have no  
597 competing interests.

598 **References**

599

- 600 Bach, L. T., Riebesell, U., Sett, S., Febiri, S., Rzepka, P., & Schulz, K. G. (2012). An approach for particle sinking  
601 velocity measurements in the 3–400  $\mu\text{m}$  size range and considerations on the effect of temperature  
602 on sinking rates. *Marine Biology*, 159(8), 1853–1864. <https://doi.org/10.1007/s00227-012-1945-2>
- 603 Badjatya, P., Akca, A. H., Fraga Alvarez, D. V., Chang, B., Ma, S., Pang, X., Wang, E., van Hinsberg, Q., Esposito,  
604 D. V., & Kawashima, S. (2022). Carbon-negative cement manufacturing from seawater-derived  
605 magnesium feedstocks. *Proc Natl Acad Sci U S A*, 119(34), e2114680119.  
606 <https://doi.org/https://doi.org/10.1073/pnas.2114680119>
- 607 Berner, R. A. (1975). The role of magnesium in the crystal growth of calcite and aragonite from sea water.  
608 *Geochimica et Cosmochimica Acta*, 39(4), 489–504. [https://doi.org/https://doi.org/10.1016/0016-](https://doi.org/https://doi.org/10.1016/0016-7037(75)90102-7)  
609 [7037\(75\)90102-7](https://doi.org/https://doi.org/10.1016/0016-7037(75)90102-7)
- 610 Bialik, O. M., Sisma-Ventura, G., Vogt-Vincent, N., Silverman, J., & Katz, T. (2022). Role of oceanic abiotic  
611 carbonate precipitation in future atmospheric CO<sub>2</sub> regulation. *Sci Rep*, 12(1), 15970.  
612 <https://doi.org/https://doi.org/10.1038/s41598-022-20446-7>
- 613 Broecker, W. S., & Takahashi, T. (1966). Calcium carbonate precipitation on the Bahama Banks. *Journal of*  
614 *Geophysical Research*, 71(6), 1575–1602. <https://doi.org/https://doi.org/10.1029/JZ071i006p01575>
- 615 Brunauer, S., Emmett, P. H., & Teller, E. (1938). Adsorption of gases in multimolecular layers. *Journal of the*  
616 *American chemical society*, 60(2), 309–319.
- 617 Burton, E. A., & Walter, L. M. (1990). The role of pH in phosphate inhibition of calcite and aragonite  
618 precipitation rates in seawater. *Geochimica et Cosmochimica Acta*, 54(3), 797–808.  
619 [https://doi.org/https://doi.org/10.1016/0016-7037\(90\)90374-T](https://doi.org/https://doi.org/10.1016/0016-7037(90)90374-T)
- 620 Bustos-Serrano, H., Morse, J. W., & Millero, F. J. (2009). The formation of whittings on the Little Bahama Bank.  
621 *Marine Chemistry*, 113(1-2), 1–8. <https://doi.org/https://doi.org/10.1016/j.marchem.2008.10.006>
- 622 Caserini, S., Pagano, D., Campo, F., Abbà, A., De Marco, S., Righi, D., Renforth, P., & Grosso, M. (2021). Potential  
623 of Maritime Transport for Ocean Liming and Atmospheric CO<sub>2</sub> Removal. *Frontiers in Climate*, 3.  
624 <https://doi.org/https://doi.org/10.3389/fclim.2021.575900>
- 625 Chave, K. E., & Suess, E. (1970). Calcium Carbonate Saturation in Seawater: Effects of Dissolved Organic Matter.  
626 *Limnology and Oceanography*, 15(4), 633–637.  
627 <https://doi.org/https://doi.org/10.4319/lo.1970.15.4.0633>
- 628 Eisaman, M., Geilert, S., Renforth, P., Bastianini, L., Campbell, J., Dale, A., Foteinis, S., Grasse, P., Hawrot, O., &  
629 Löscher, C. (2023). Chapter 3: Assessing the technical aspects of OAE approaches. *State of the Planet*  
630 *Discussions*, 2023, 1–52. <https://doi.org/https://doi.org/10.5194/sp-2-oae2023-3-2023>
- 631 Faucher, G., Haunost, M., Paul, A. J., Tietz, A. U. C., & Riebesell, U. (2025). Growth response of *Emiliania huxleyi*  
632 to ocean alkalinity enhancement. *Biogeosciences*, 22(2), 405–415. [https://doi.org/10.5194/bg-22-405-](https://doi.org/10.5194/bg-22-405-2025)  
633 [2025](https://doi.org/10.5194/bg-22-405-2025)
- 634 Ferderer, A., Chase, Z., Kennedy, F., Schulz, K. G., & Bach, L. T. (2022). Assessing the influence of ocean  
635 alkalinity enhancement on a coastal phytoplankton community. *Biogeosciences*, 19(23), 5375–5399.  
636 <https://doi.org/10.5194/bg-19-5375-2022>
- 637 Fuhr, M., Geilert, S., Schmidt, M., Liebetrau, V., Vogt, C., Ledwig, B., & Wallmann, K. (2022). Kinetics of Olivine  
638 Weathering in Seawater: An Experimental Study. *Frontiers in Climate*, 4.  
639 <https://doi.org/https://doi.org/10.3389/fclim.2022.831587>
- 640 Fuss, S., Lamb, W. F., Callaghan, M. W., Hilaire, J., Creutzig, F., Amann, T., Beringer, T., de Oliveira Garcia, W.,  
641 Hartmann, J., Khanna, T., Luderer, G., Nemet, G. F., Rogelj, J., Smith, P., Vicente, J. L. V., Wilcox, J., del  
642 Mar Zamora Dominguez, M., & Minx, J. C. (2018). Negative emissions—Part 2: Costs, potentials and  
643 side effects. *Environmental Research Letters*, 13(6). <https://doi.org/10.1088/1748-9326/aabf9f>
- 644 Gately, J. A., Kim, S. M., Jin, B., Brzezinski, M. A., & Iglesias-Rodriguez, M. D. (2023). Coccolithophores and  
645 diatoms resilient to ocean alkalinity enhancement: A glimpse of hope? *Science Advances*, 9(24),  
646 eadg6066. <https://doi.org/10.1126/sciadv.adg6066>
- 647 Goldenberg, S. U., Riebesell, U., Brüggemann, D., Börner, G., Sswat, M., Folkvord, A., Couret, M., Spjelkavik, S.,  
648 Sánchez, N., Jaspers, C., & Moyano, M. (2024). Early life stages of fish under ocean alkalinity  
649 enhancement in coastal plankton communities. *Biogeosciences*, 21(20), 4521–4532.  
650 <https://doi.org/10.5194/bg-21-4521-2024>

651 Haas, A. R. (1916). The Effect of the Addition of Alkali to Sea Water Upon the Hydrogen Ion Concentration.  
652 *Journal of Biological Chemistry*, 26(2), 515–517. [https://doi.org/https://doi.org/10.1016/s0021-](https://doi.org/https://doi.org/10.1016/s0021-9258(18)87433-6)  
653 [9258\(18\)87433-6](https://doi.org/https://doi.org/10.1016/s0021-9258(18)87433-6)

654 Hartmann, J., Suitner, N., Lim, C., Schneider, J., Marín-Samper, L., Arístegui, J., Renforth, P., Taucher, J., &  
655 Riebesell, U. (2023). Stability of alkalinity in ocean alkalinity enhancement (OAE) approaches –  
656 consequences for durability of CO<sub>2</sub> storage. *Biogeosciences*, 20(4), 781–802.  
657 <https://doi.org/https://doi.org/10.5194/bg-20-781-2023>

658 Hartmann, J., West, A. J., Renforth, P., Köhler, P., De La Rocha, C. L., Wolf-Gladrow, D. A., Dürr, H. H., &  
659 Scheffran, J. (2013). Enhanced chemical weathering as a geoengineering strategy to reduce  
660 atmospheric carbon dioxide, supply nutrients, and mitigate ocean acidification. *Reviews of Geophysics*,  
661 51(2), 113–149. <https://doi.org/https://doi.org/10.1002/rog.20004>

662 Harvey, L. D. D. (2008). Mitigating the atmospheric CO<sub>2</sub> increase and ocean acidification by adding limestone  
663 powder to upwelling regions. *Journal of Geophysical Research: Oceans*, 113(C4).  
664 <https://doi.org/10.1029/2007jc004373>

665 He, J., & Tyka, M. D. (2023). Limits and CO<sub>2</sub> equilibration of near-coast alkalinity enhancement. *Biogeosciences*,  
666 20(1), 27–43. <https://doi.org/https://doi.org/10.5194/bg-20-27-2023>

667 Ilyina, T., Six, K. D., Segsneider, J., Maier-Reimer, E., Li, H., & Núñez-Riboni, I. (2013). Global ocean  
668 biogeochemistry model HAMOCC: Model architecture and performance as component of the MPI-  
669 Earth system model in different CMIP5 experimental realizations. *Journal of Advances in Modeling*  
670 *Earth Systems*, 5(2), 287–315. <https://doi.org/https://doi.org/10.1029/2012ms000178>

671 Inskeep, W. P., & Bloom, P. R. (1985). An evaluation of rate equations for calcite precipitation kinetics at pCO<sub>2</sub>  
672 less than 0.01 atm and pH greater than 8. *Geochimica et Cosmochimica Acta*, 49(10), 2165–2180.  
673 [https://doi.org/https://doi.org/10.1016/0016-7037\(85\)90074-2](https://doi.org/https://doi.org/10.1016/0016-7037(85)90074-2)

674 IPCC. (2023). Technical Summary. In *Climate Change 2021 – The Physical Science Basis* (pp. 35–144).  
675 <https://doi.org/10.1017/9781009157896.002>

676 Iyer, G., Hultman, N., Eom, J., McJeon, H., Patel, P., & Clarke, L. (2015). Diffusion of low-carbon technologies  
677 and the feasibility of long-term climate targets. *Technological Forecasting and Social Change*, 90, 103–  
678 118. <https://doi.org/10.1016/j.techfore.2013.08.025>

679 Kapp, E. M. (1928). The precipitation of calcium and magnesium from sea water by sodium hydroxide. *The*  
680 *Biological Bulletin*, 55(6), 453–458.

681 Kellock, C., Castillo Alvarez, M. C., Finch, A., Penkman, K., Kroger, R., Clog, M., & Allison, N. (2022). Optimising a  
682 method for aragonite precipitation in simulated biogenic calcification media. *PLoS One*, 17(12),  
683 e0278627. <https://doi.org/https://doi.org/10.1371/journal.pone.0278627>

684 Kheshti, H. S. (1995). Sequestering atmospheric carbon dioxide by increasing ocean alkalinity. *Energy*, 20(9),  
685 915–922. [https://doi.org/https://doi.org/10.1016/0360-5442\(95\)00035-F](https://doi.org/https://doi.org/10.1016/0360-5442(95)00035-F)

686 Marín-Samper, L., Arístegui, J., Hernández-Hernández, N., Ortiz, J., Archer, S. D., Ludwig, A., & Riebesell, U.  
687 (2024). Assessing the impact of CO<sub>2</sub>-equilibrated ocean alkalinity enhancement on microbial  
688 metabolic rates in an oligotrophic system. *Biogeosciences*, 21(11), 2859–2876.  
689 <https://doi.org/10.5194/bg-21-2859-2024>

690 Marion, G., Millero, F., & Feistel, R. (2009). Precipitation of solid phase calcium carbonates and their effect on  
691 application of seawater S A–T–P models. *Ocean science*, 5(3), 285–291.  
692 <https://doi.org/https://doi.org/10.5194/os-5-285-2009>

693 Minx, J. C., Lamb, W. F., Callaghan, M. W., Fuss, S., Hilaire, J., Creutzig, F., Amann, T., Beringer, T., de Oliveira  
694 Garcia, W., Hartmann, J., Khanna, T., Lenzi, D., Luderer, G., Nemet, G. F., Rogelj, J., Smith, P., Vicente  
695 Vicente, J. L., Wilcox, J., & del Mar Zamora Dominguez, M. (2018). Negative emissions—Part 1:  
696 Research landscape and synthesis. *Environmental Research Letters*, 13(6).  
697 <https://doi.org/10.1088/1748-9326/aabf9b>

698 Moras, C. A., Bach, L. T., Cyronak, T., Joannes-Boyau, R., & Schulz, K. G. (2022). Ocean alkalinity enhancement –  
699 avoiding runaway CaCO<sub>3</sub> precipitation during quick and hydrated lime dissolution. *Biogeosciences*,  
700 19(15), 3537–3557. <https://doi.org/https://doi.org/10.5194/bg-19-3537-2022>

701 Moras, C. A., Cyronak, T., Bach, L. T., Joannes-Boyau, R., & Schulz, K. G. (2024). Effects of grain size and  
702 seawater salinity on magnesium hydroxide dissolution and secondary calcium carbonate precipitation  
703 kinetics: implications for ocean alkalinity enhancement. *Biogeosciences*, 21(14), 3463–3475.  
704 <https://doi.org/10.5194/bg-21-3463-2024>

705 Morse, J. W., Arvidson, R. S., & Lüttge, A. (2007). Calcium carbonate formation and dissolution. *Chemical*  
706 *reviews*, 107(2), 342–381. <https://doi.org/https://doi.org/10.1021/cr050358j>

- 707 Morse, J. W., Gledhill, D. K., & Millero, F. J. (2003). CaCO<sub>3</sub> precipitation kinetics in waters from the great  
708 Bahama bank. *Geochimica et Cosmochimica Acta*, 67(15), 2819–2826.  
709 [https://doi.org/https://doi.org/10.1016/s0016-7037\(03\)00103-0](https://doi.org/https://doi.org/10.1016/s0016-7037(03)00103-0)
- 710 Morse, J. W., & He, S. (1993). Influences of T, S and PCO<sub>2</sub> on the pseudo-homogeneous precipitation of CaCO<sub>3</sub>  
711 from seawater: implications for whiting formation. *Marine Chemistry*, 41(4), 291–297.  
712 [https://doi.org/https://doi.org/10.1016/0304-4203\(93\)90261-L](https://doi.org/https://doi.org/10.1016/0304-4203(93)90261-L)
- 713 Mucci, A., & Morse, J. W. (1983). The incorporation of Mg<sup>2+</sup> and Sr<sup>2+</sup> into calcite overgrowths: influences of  
714 growth rate and solution composition. *Geochimica et Cosmochimica Acta*, 47(2), 217–233.  
715 [https://doi.org/https://doi.org/10.1016/0016-7037\(83\)90135-7](https://doi.org/https://doi.org/10.1016/0016-7037(83)90135-7)
- 716 Oschlies, A., Bach, L. T., Rickaby, R. E. M., Satterfield, T., Webb, R., & Gattuso, J.-P. (2023). Climate targets,  
717 carbon dioxide removal, and the potential role of ocean alkalinity enhancement. *State of the Planet*, 2-  
718 *oae2023*, 1–9. <https://doi.org/10.5194/sp-2-oae2023-1-2023>
- 719 Ou, Y., Xue, Z. G., & Hu, X. (2025). A numerical assessment of ocean alkalinity enhancement efficiency on a  
720 river-dominated continental shelf – a case study in the northern Gulf of Mexico. *Environmental*  
721 *Research Letters*. <https://doi.org/10.1088/1748-9326/adaa8b>
- 722 Pan, Y., Li, Y., Ma, Q., He, H., Wang, S., Sun, Z., Cai, W.-J., Dong, B., Di, Y., Fu, W., & Chen, C.-T. A. (2021). The  
723 role of Mg<sup>2+</sup> in inhibiting CaCO<sub>3</sub> precipitation from seawater. *Marine Chemistry*, 237.  
724 <https://doi.org/https://doi.org/10.1016/j.marchem.2021.104036>
- 725 Paul, A. J., Haunost, M., Goldenberg, S. U., Hartmann, J., Sanchez, N. S., Schneider, J., Suitner, N., & Riebesell, U.  
726 (2024). Ocean alkalinity enhancement in an open ocean ecosystem: Biogeochemical responses and  
727 carbon storage durability. *EGUsphere*. <https://doi.org/https://doi.org/10.5194/egusphere-2024-417>
- 728 Pokrovsky, O. S. (1998). Precipitation of calcium and magnesium carbonates from homogeneous  
729 supersaturated solutions. *Journal of Crystal Growth*, 186(1-2), 233–239.  
730 [https://doi.org/https://doi.org/10.1016/S0022-0248\(97\)00462-4](https://doi.org/https://doi.org/10.1016/S0022-0248(97)00462-4)
- 731 Pytkowicz, R. (1973). Calcium carbonate retention in supersaturated seawater. *American Journal of Science*,  
732 273(6), 515–522. <https://doi.org/http://dx.doi.org/10.2475/ajs.273.6.515>
- 733 Pytkowicz, R. M. (1965). Rates of Inorganic Calcium Carbonate Nucleation. *The Journal of Geology*, 73(1), 196–  
734 199. <https://doi.org/10.1086/627056>
- 735 Ramírez, L., Pozzo-Pirotta, L. J., Trebec, A., Manzanares-Vázquez, V., Díez, J. L., Arístegui, J., Riebesell, U.,  
736 Archer, S. D., & Segovia, M. (2024). Ocean Alkalinity Enhancement (OAE) does not cause cellular stress  
737 in a phytoplankton community of the sub-tropical Atlantic Ocean. *EGUsphere*, 2024, 1–34.  
738 <https://doi.org/https://doi.org/10.5194/egusphere-2024-847>
- 739 Rau, G. H., & Caldeira, K. (1999). Enhanced carbonate dissolution as a means of sequestering carbon dioxide in  
740 the ocean. *Energy Conversion and Management*, 40(17), 1803–1813. [https://doi.org/10.1016/S0196-8904\(99\)00071-0](https://doi.org/10.1016/S0196-8904(99)00071-0)
- 741
- 742 Renforth, P., & Henderson, G. (2017). Assessing ocean alkalinity for carbon sequestration. *Reviews of*  
743 *Geophysics*, 55(3), 636–674. <https://doi.org/https://doi.org/10.1002/2016rg000533>
- 744 Ringham, M. C., Hirtle, N., Shaw, C., Lu, X., Herndon, J., Carter, B. R., & Eisaman, M. D. (2024). An assessment of  
745 ocean alkalinity enhancement using aqueous hydroxides: kinetics, efficiency, and precipitation  
746 thresholds. *Biogeosciences*, 21(15), 3551–3570. <https://doi.org/https://doi.org/10.5194/bg-21-3551-2024>
- 747
- 748 Rogelj, J., Popp, A., Calvin, K. V., Luderer, G., Emmerling, J., Gernaat, D., Fujimori, S., Strefler, J., Hasegawa, T.,  
749 Marangoni, G., Krey, V., Kriegler, E., Riahi, K., van Vuuren, D. P., Doelman, J., Drouet, L., Edmonds, J.,  
750 Fricko, O., Harmsen, M.,...Tavoni, M. (2018). Scenarios towards limiting global mean temperature  
751 increase below 1.5 °C. *Nature Climate Change*, 8(4), 325–332. <https://doi.org/10.1038/s41558-018-0091-3>
- 752
- 753 Schulz, K. G., Bach, L. T., & Dickson, A. G. (2023). Seawater carbonate chemistry considerations for ocean  
754 alkalinity enhancement research: theory, measurements, and calculations. *Guide to Best Practices in*  
755 *Ocean Alkalinity Enhancement Research*, 2-oae2023, 2. <https://doi.org/10.5194/sp-2-oae2023-2-2023>
- 756 Schwinger, J., Bourgeois, T., & Rickels, W. (2024). On the emission-path dependency of the efficiency of ocean  
757 alkalinity enhancement. *Environmental Research Letters*, 19(7). <https://doi.org/10.1088/1748-9326/ad5a27>
- 758
- 759 Sers, M. R., & Victor, P. A. (2018). The Energy-emissions Trap. *Ecological Economics*, 151, 10–21.  
760 <https://doi.org/10.1016/j.ecolecon.2018.04.004>
- 761 Sjöberg, E. (1976). A fundamental equation for calcite dissolution kinetics. *Geochimica et Cosmochimica Acta*,  
762 40(4), 441–447. [https://doi.org/https://doi.org/10.1016/0016-7037\(76\)90009-0](https://doi.org/https://doi.org/10.1016/0016-7037(76)90009-0)
- 763 Söhnle, O., & Mullin, J. W. (1988). Interpretation of crystallization induction periods. *Journal of colloid and*  
764 *interface science*, 123(1), 43–50. [https://doi.org/https://doi.org/10.1016/0021-9797\(88\)90219-6](https://doi.org/https://doi.org/10.1016/0021-9797(88)90219-6)

765 Suessle, P., Taucher, J., Goldenberg, S., Baumann, M., Spilling, K., Noche-Ferreira, A., Vanharanta, M., &  
766 Riebesell, U. (2023). Particle fluxes by subtropical pelagic communities under ocean alkalinity  
767 enhancement. *EGUsphere*, 2023, 1–26. <https://doi.org/https://doi.org/10.5194/egusphere-2023-2800>

768 Suitner, N., Faucher, G., Lim, C., Schneider, J., Moras, C. A., Riebesell, U., & Hartmann, J. (2024). Ocean alkalinity  
769 enhancement approaches and the predictability of runaway precipitation processes: results of an  
770 experimental study to determine critical alkalinity ranges for safe and sustainable application  
771 scenarios. *Biogeosciences*, 21(20), 4587–4604. <https://doi.org/10.5194/bg-21-4587-2024>

772 Tjørve, K. M., & Tjørve, E. (2017). The use of Gompertz models in growth analyses, and new Gompertz-model  
773 approach: An addition to the Unified-Richards family. *PLoS One*, 12(6), e0178691.  
774 <https://doi.org/https://doi.org/10.1371/journal.pone.0178691>

775 UNFCCC. (2015). Report of the Conference of the Parties to the United Nations Framework Convention on  
776 Climate Change (21st Session, 2015: Paris). Retrived December. Vol. 4. 2015.

777 Varliero, S., Buono, A., Caserini, S., Raos, G., & Macchi, P. (2024). Chemical Aspect of Ocean Liming for CO2  
778 Removal: Dissolution Kinetics of Calcium Hydroxide in Seawater. *ACS Engineering Au*.  
779 <https://doi.org/https://doi.org/10.1021/acsengineeringau.4c00008>

780 Wang, H., Pilcher, D. J., Kearney, K. A., Cross, J. N., Shugart, O. M., Eisaman, M. D., & Carter, B. R. (2023).  
781 Simulated impact of ocean alkalinity enhancement on atmospheric CO2 removal in the Bering Sea.  
782 *Earth's Future*, 11(1). [https://doi.org/ https://doi.org/10.1029/2022EF002816](https://doi.org/https://doi.org/10.1029/2022EF002816)

783 Wells, M. L., & Goldberg, E. D. (1992). Marine submicron particles. *Marine Chemistry*, 40(1-2), 5–18.  
784 [https://doi.org/https://doi.org/10.1016/0304-4203\(92\)90045-C](https://doi.org/https://doi.org/10.1016/0304-4203(92)90045-C)

785 Wurgaft, E., Steiner, Z., Luz, B., & Lazar, B. (2016). Evidence for inorganic precipitation of CaCO3 on suspended  
786 solids in the open water of the Red Sea. *Marine Chemistry*, 186, 145–155.  
787 <https://doi.org/https://doi.org/10.1016/j.marchem.2016.09.006>

788 Wurgaft, E., Wang, Z. A., Churchill, J. H., Dellapenna, T., Song, S., Du, J., Ringham, M. C., Rivlin, T., & Lazar, B.  
789 (2021). Particle Triggered Reactions as an Important Mechanism of Alkalinity and Inorganic Carbon  
790 Removal in River Plumes. *Geophysical Research Letters*, 48(11), 277.  
791 <https://doi.org/https://doi.org/10.1029/2021gl093178>

792 Xin, X., Goldenberg, S. U., Taucher, J., Stühr, A., Aristegui, J., & Riebesell, U. (2024). Resilience of Phytoplankton  
793 and Microzooplankton Communities under Ocean Alkalinity Enhancement in the Oligotrophic Ocean.  
794 *Environ Sci Technol*. <https://doi.org/10.1021/acs.est.4c09838>

795 Zeebe, R., & Wolf-Gladrow, D. (2001). *CO2 in Seawater: Equilibrium, Kinetics, Isotopes*. Elsevier Oceanography  
796 Book Series. 65.

797 Zhong, S., & Mucci, A. (1989). Calcite and aragonite precipitation from seawater solutions of various salinities:  
798 Precipitation rates and overgrowth compositions. *Chemical geology*, 78(3-4), 283–299.  
799 [https://doi.org/https://doi.org/10.1016/0009-2541\(89\)90064-8](https://doi.org/https://doi.org/10.1016/0009-2541(89)90064-8)

800 Zhou, M., Tyka, M. D., Ho, D. T., Yankovsky, E., Bachman, S., Nicholas, T., Karspeck, A. R., & Long, M. C. (2024).  
801 Mapping the global variation in the efficiency of ocean alkalinity enhancement for carbon dioxide  
802 removal. *Nature Climate Change*, 1–7. <https://doi.org/https://doi.org/10.1038/s41558-024-02179-9>

803